2007-09-11

Numerical Simulation of Vortex Generating Jets in Zero and Adverse Pressure Gradients

Curtis Lynn Memory
Brigham Young University - Provo

NUMERICAL SIMULATION OF VORTEX GENERATING JETS IN ZERO AND ADVERSE PRESSURE GRADIENTS

by

Curtis L. Memory

A thesis submitted to the faculty of

Brigham Young University

in partial fulfillment of the requirements for the degree of

Master of Science

Department of Mechanical Engineering

Brigham Young University

December 2007

BRIGHAM YOUNG UNIVERSITY

GRADUATE COMMITTEE APPROVAL

of a thesis submitted by

Curtis L. Memory

This thesis has been read by each member of the following graduate committee and by majority vote has been found to be satisfactory.

Date	Deryl O. Snyder, Chair
Date	Scott L. Thomson
Date	W. Jerry Bowman

BRIGHAM YOUNG UNIVERSITY

As chair of the candidate's graduate committee, I have read the thesis of Curtis L. Memory in its final form and have found that (1) its format, citations, and bibliographical style are consistent and acceptable and fulfill university and department style requirements; (2) its illustrative materials including figures, tables, and charts are in place; and (3) the final manuscript is satisfactory to the graduate committee and is ready for submission to the university library.

Date

Deryl O. Snyder
Chair, Graduate Committee

Accepted for the Department

Matthew R. Jones
Graduate Coordinator

Accepted for the College

Alan R. Parkinson
Dean, Ira A. Fulton College of
Engineering and Technology

ABSTRACT

NUMERICAL SIMULATION OF VORTEX GENERATING JETS IN ZERO AND ADVERSE PRESSURE GRADIENTS

Curtis L. Memory

Department of Mechanical Engineering

Master of Science

Numerical simulations of particle image velocimetry (PIV) experiments conducted with vortex generating jets (VGJs) on a flat plate, at a Reynolds number based on plate length of 50,000, were performed for three flow conditions using a time-accurate hybrid Navier-Stokes solver. Time-averaged steady blowing of angled jets, subjected to a zero pressure gradient, yielded excellent agreement with the PIV data in terms of vortex formation and strength. Observed flow features include primary and secondary vortices, where the primary vortex eventually dominates the downstream region. A shell wall structure, created by smaller vortical structures surrounding the developing vortices, was also observed. A pulsed jet in a zero pressure gradient was then initialized from a no-control case. A qualitative comparison between averaged experimental and instantaneous numerical results was performed with

good agreement in terms of the convected size and distance of the wake. Analysis of the instantaneous numerical flow field agreed well with various flow visualization experiments describing the formation of "kidney" vortices. Various indicators point to the production of a primary vortex by the reduced mass flow of the pulsed jet. Finally, an adverse pressure gradient was applied, inducing a laminar separation zone on the plate. A pulsed angled jet induced strong spanwise vortices in the separated shear layer which appear to weaken the separation zone and allow the bulk jet fluid to flush the remaining low-momentum fluid out of the domain. It is reasonable to assume that reduced blowing ratios and duty cycles would produce similar shear layer vortices and comparable loss reductions. Influences of both turbulent transition and dominant vortical structures were observed, though the spanwise shear layer vortices appear to be critical to the laminar separation reduction scenarios observed in this study.

ACKNOWLEDGMENTS

I am indebted to my advisor, Dr. Deryl Snyder for his seemingly endless patience through so many questions. I have greatly enjoyed his help, guidance, and friendship. Also, this project would not have flown as smoothly without the help of Tom Raisor and Lloyd Brown of the Supercomputing Lab.

The help and comfort of so many friends, within the college and without, is too numerous to mention individually and has been often needed and always greatly appreciated. Finally, I am eternally grateful for my family, both immediate and extended, which have shown nothing but open love and support, for as long as I am able to remember.

Table of Contents

List of Tables

List of Figures

Chapter 1

Introduction

Low pressure turbine (LPT) blades are a crucial component in the design of a gas turbine. The operational Reynolds numbers experienced by some gas turbines during missions involving high altitude cruise ($\sim$25,000), places these blades in a regime where laminar boundary layer separation is often present. Component losses resulting from laminar separation potentially reach up to 7% for small military engines at high altitude, compared to low altitude performance of the same [1]. Methods for mitigating separation effects are an active area of research and are divided into two major categories. Passive controls, such as surface protrusions or recessions, are typically optimized for a specific operating condition which can, in turn, adversely affect performance during other stages in a mission. Active flow controls such as vortex generating jets (VGJs) have been shown to successfully manage laminar separation and could be adjusted during operation, depending on mission conditions. In light of the numerous variables influencing VGJ performance, ranging from jet duration to jet velocity relative to the free stream (blowing ratio), it is clear that application of VGJs is a complex problem.

One such variable, pulsing of the jet, has been established as an important factor in VGJ performance. Experiments by various researchers have shown that the reduced mass flow of a pulsed jet can mitigate separation losses just as effectively as a steady jet [2, 3, 4]. This is significant due to reduced inefficiencies related to bleed losses for other components in the engine when providing massflow for the jet. However, the mechanisms behind the efficacy of a pulsed jet are still under scrutiny. Steady jets have been shown to eliminate separation primarily by mixing high momentum free stream fluid with boundary layer fluid by means of longitudinal

vortices propagating downstream of the jet [5, 6, 7]. Conversely, the transient pulsed jet does not exhibit the same trends in structure and many researchers attribute the primary mechanism to boundary layer transition to turbulence and subsequent reattachment. Directly linked to pulsing is the selection of frequency and duty cycle (ratio of pulse period to jet-on time) which was evaluated by Bons et al. [2, 3]. These studies, performed in a blade cascade, found ranges of frequencies, duty cycles, and blowing ratios at which separation losses are significantly reduced.

Another example of the complexity involved when implementing VGJs is found in the similarities in mechanical implementation shared between VGJs and film cooling systems, the latter already a common feature to gas turbines. Haven and Kurosaka [8] note that some vortical structures inherent to many cross flow jets can actually inhibit the film cooling process because of their tendency to lift the jet fluid away from the blade wall. The ability to confidently simulate the flow in direct proximity to the VGJ with high resolution, greatly aids the analysis of such flow features. The variables discussed above are only a portion of the factors influencing VGJ efficiency.

Numerical simulations of cross flow jets have been performed by many researchers. Yuan et al. [9] performed large eddy simulations on a vertical jet and observed the characteristic counter rotating vortex pair as well as various other vortical structures surrounding the jet fluid. Jiang and Liu [10] evaluated pulsed jets on a NACA 0012 airfoil using direct numeric simulations and made observations about separation reduction, similar to those found in the pulsed turbine cascade experiments mentioned above. Rizzetta and Visbal [11] performed direct numeric simulations on a turbine blade and showed that transition was a key component to separation zone reduction. Postl et al. [12, 13] performed high resolution simulations of VGJs on a flat plate as well as simulations of pulsed VGJs on turbine blades. Separation control was obtained for low blowing ratios utilizing pulsing frequencies based on natural frequencies of the separated shear layer. This work has been continued more recently by Gross and Fasel [14, 15].

The above is a sample of the numerical simulations performed to date on VGJs. However, comparison and/or benchmarking against experimental data is frequently

limited, particularly in the near jet region. Increased confidence in the results of such numerical studies can be obtained by benchmarking simulations with experiments which would also readily compliment the extensive work already performed by previous researchers.

Experiments conducted by Hansen and Bons [16, 17] evaluated various VGJ settings on a flat plate using particle image velocimetry (PIV) at a Reynolds number based on plate length of 50,000. Of primary interest in these experiments was the formation of vortical structures downstream of the jet subjected to both zero and adverse pressure gradients. Various combinations of normal versus angled jets as well as steady versus pulsed jets were studied. The cumulative contribution to reducing separation flow losses induced by the adverse pressure gradient was also evaluated.

These experiments provide well-defined geometries and flow conditions with which to benchmark numerical simulations of VGJs by an in-house hybrid solver, which will be the main goal of this work. The primary focus will be to compare high resolution numerical simulations with experiments conducted for steady, angled VGJs on a flat plate under a zero pressure gradient (ZPG). A more in-depth analysis of the numerical results will also be performed. Pulsing capabilities for the angled jet will then be demonstrated in the ZPG setting. However, because of the computational requirements incurred for obtaining time averaged flow fields for the pulsed jet, only a brief qualitative comparison between averaged experimental data and instantaneous numerical data will be performed. This will be followed by a discussion of instantaneous flow features found in the numerics. An adverse pressure gradient (APG) will then be applied to the flat plate to achieve a laminar separation zone comparable to that found on a LPT blade. The experimental dimensions of the laminar separation zone are successfully matched and a pulsed jet observed and discussed. This final analysis will focus on the contributions of dominant vortical structures versus turbulent transition to reduce laminar separation in the numerical results.

Chapter 2

Experimental Setup

2.1 Flat Plate Configuration

The following chapter will briefly describe the experimental setup utilized by Hansen and Bons [16] to observe the flat plate VGJ flow fields. Detailed descriptions of the experimental configuration and equipment can be found in Hansen [17] or Eldredge [18].

The open circuit wind tunnel used in the experiments has a 0.381 m x 0.381 m x 1.83 m test section, constructed of clear acrylic plastic to allow laser beam passage as well as provide views for digital cameras for optical flow measurements. The tunnel is capable of mass flows up to 3 kg/s. Various flow treatments are applied upstream of the test section, reducing free stream turbulence levels to less than 0.3%. Tunnel construction readily facilitates integration of a variety of components to obtain a range of flow conditions within the test section.

VGJs normal to the flow were created by drilling 4mm diameter holes vertically into an acrylic plate. The same diameter drill stretched the circles to 4 mm x 8 mm

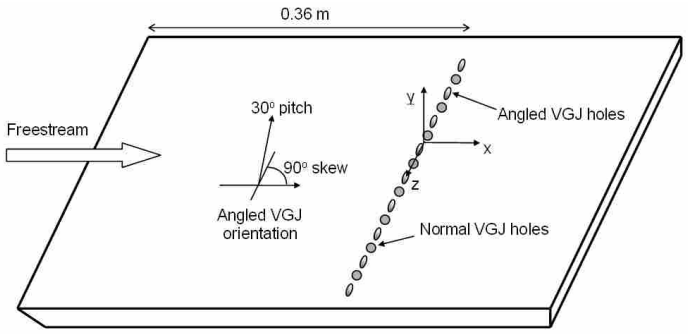

Figure 2.1: Schematic of flat plate setup, showing flow and jet direction relative to free stream. Modified from Hansen and Bons [16].

ovals when creating the angled holes as shown in Figure 2.1. These holes were skewed 90° to the free stream and pitched 30° from the xz plane. All holes were placed 0.36 m from the leading edge of the plate and horizontally spaced $10d$ from the nearest neighbor of the same type. The normal holes were covered with tape when not in use. The VGJ plate was elevated away from the tunnel wall to facilitate boundary layer growth similar to that found on a LPT blade. Reynolds number based on the inlet velocity and the streamwise distance from the leading edge of the plate was 50,000. The flat plate configuration was utilized to evaluate the VGJ flow field isolated from other flow influences.

2.2 Wedge Configuration

To obtain a laminar separation zone comparable to that found on a LPT blade, an adverse pressure gradient was induced on the flat plate by introducing a foam wedge on the opposite wall from the VGJ plate, as shown in Figure 2.2. The wedge configuration is similar to that used by Volino and Hultgren [1], and successfully simulates a pressure gradient similar to that found on the PackB LPT airfoil. This airfoil was chosen primarily because of its frequent use in LPT blade research at these Reynolds numbers. The wedge created a throat 0.15 m tall and an inlet 0.34 m

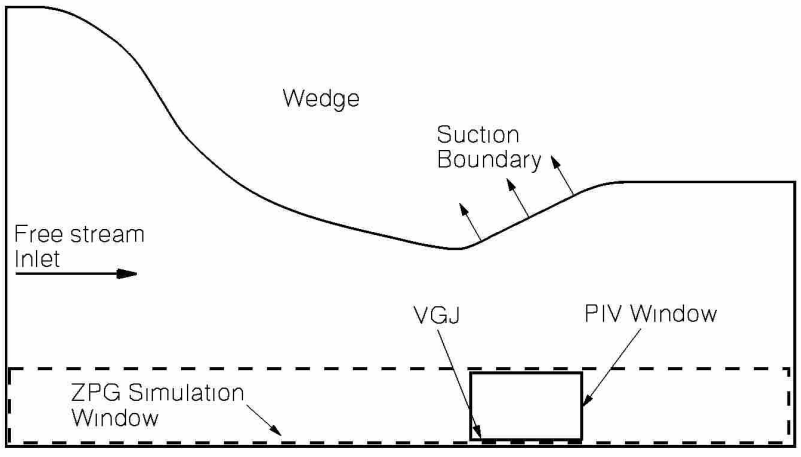

Figure 2.2: Schematic of wedge configuration showing suction boundary and data windows for PIV measurements and ZPG numerical simulations.

tall. The influence of flow separation at the wedge throat was eliminated by first, covering the wall upstream of the throat with sand paper in an attempt to transition the boundary layer to turbulent and second, by applying suction directly aft of the throat, as seen along the wedge wall in Figure 2.2. The desired pressure gradient distribution was found by iterating on combinations of suction strength and wedge position in the x direction. These iterations resulted in the throat sitting 0.01 m upstream of the VGJ holes.

The pressure gradient was verified with the method specified by Volino and Hultgren [1] who calculated the coefficient of pressure as shown in Eq. 2.1.

$$C_p = 1 - \left(\frac{U_e}{U_{ex}}\right)^2 \tag{2.1}$$

In these experiments U_{ex} was the channel exit velocity and U_e, the boundary layer edge velocity, was acquired by traversing the flat plate in the x direction at y/d=15 at the mid-span location with a single element hot wire. This height was chosen in order to avoid the influence of the developing boundary layer while still measuring a representative edge velocity. The resulting C_p distribution will be presented in Chapter 5, in conjunction with the numerical simulation results.

2.3 Particle Image Velocimetry

Three-component particle image velocimetry (PIV) measurements were obtained by illuminating two dimensional slices of the flow field with a green Nd:YAG laser sheet oriented in the xy plane, normal to the plate, as shown in Figure 2.3. Two cameras were positioned in a stereo configuration outside the tunnel walls, normal to the laser sheet, aimed along the z axis. The cameras were oriented to obtain a data window 90 mm in the x direction by 70 mm in the y direction. The tunnel flow was seeded upstream of the test section with atomized olive oil, created by injecting a high speed air jet into an oil reservoir which was connected to the tunnel with a plastic tube.

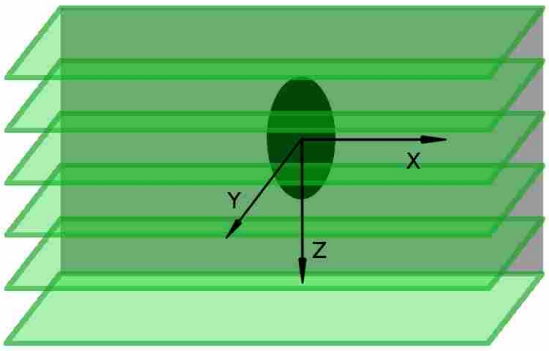

Figure 2.3: Schematic of xy plane laser sheet orientation relative to hole.

Data acquisition began at a mid-pitch hole location and proceeded in the z direction at 2 mm increments until the full VGJ had been covered. A LaVision post processing package then calculated average u, v, and w components for each plane. It was found that 40 images of each xy plane was sufficient for an averaged flow field at each z location. A typical data set consisted of 21 xy planes for a single hole. Velocity uncertainty was estimated at $\pm$ 0.1 m/s based on a seed particle position uncertainty of 0.1 image pixels, as declared by the software vendor.

A Matlab script was then used to combine the velocities from each xy plane into one three-dimensional data block as well as normalize the velocity components with the free stream velocity. Physical space coordinates were normalized with respect to hole diameter and shifted such that the holes were located at x/d=0, y/d=0, and z/d=10 in the analysis plots. Matlab then calculated vorticity about all three axes at all points in the block and was utilized to post-process the data set by extracting two-dimensional contour plots and three-dimensional velocity iso-surface plots. For this study the same script was used to prepare the data sets for analysis, with the exception of the plot generation functions. It was slightly modified to export the data in a format usable by the commercial post-processing package Tecplot, to maintain consistency with the data file format of the numerical solver. Also, the script was modified to shift the VGJ hole location in the spanwise direction to z/d=8.5.

2.4 VGJ Characteristics

Common to both pressure gradient settings is the assignment of jet characteristics. The jet exit velocity is typically represented in terms of a blowing ratio, B, which is defined as the ratio of the jet exit velocity to the free stream velocity above the jet hole. Bons et al. [2, 3] found that a blowing ratio between 2 and 4 was most effective for separation reduction. The lower end of this range was selected in order to minimize compressed air requirements to the tunnel. Three blowing ratios were evaluated in these experiments. The steady zero pressure gradient case was set to B=2 and increased to B=2.5 for pulsing. The pulsed adverse pressure gradient case was conducted at B=3.

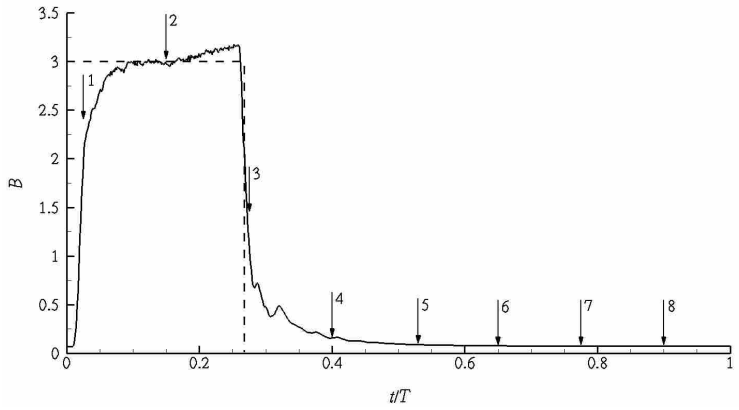

Figure 2.4: Example pulse history for one pulse period at B=3. Phase locations indicated by arrows. Dashed line represents pulse step function used in numerical simulations.

Other significant components of these experiments was the assignment of pulsing variables. A pulse frequency of 5 Hz was selected, which resulted in a non-dimensional frequency of 0.34, as defined by

$$F^{+} = \frac{0.41f}{U_{in}/C_x}, \tag{2.2}$$

where f is the pulsing frequency, U_{in} the inlet velocity, and C_x the axial chord, or in the case of the flat plate, the distance from the leading edge of the plate to the holes. The duty cycle (ratio of on-time to pulse period) was set to 25%. These pulse settings were used for both the ZPG and APG configurations.

Specific points in the pulse period were analyzed with a phase-locked averaging method. The PIV system was synchronized with the VGJ pulse so that the laser was fired at specific moments during the pulse period, referred to as phases. The eight phases analyzed in this study are plotted in Figure 2.4 along with a sample pulse history at a maximum B of three. Phases were chosen such that the beginning, middle, and end of a jet pulse as well as various intervals of wake propagation downstream, could be analyzed. The full flow field at each phase was acquired by the PIV system following the procedure used for the the steady jet.

Chapter 3

Numerical Method

3.1 Numerical Solver

3.1.1 Method and Formulation

A time-accurate hybrid LES/DNS solver called Spectral Finite Element Large Eddy Simulation (SFELES) was chosen for the VGJ simulations. It solves the unsteady incompressible Navier Stokes equations using a second order finite element method in the xy plane, and a Fourier method in the spanwise or z direction. This method lends well to solving flow fields around two-dimensional geometries that are characterized by periodic three-dimensional flow features in the z direction. Various benefits stem from this method which will be discussed in this section. For detailed descriptions of the solver formulation, the reader is directed to Snyder and Degrez [19, 20].

The laminar, incompressible, and isothermal Navier Stokes equations with no body forces are defined in vector notation as

$$\frac{\partial \overrightarrow{u}}{\partial t} + (\overrightarrow{u} \cdot \nabla)\overrightarrow{u} = -\nabla p + \nu \nabla^2 \overrightarrow{u}. \tag{3.1}$$

The continuity equation is defined as

$$\nabla \cdot \overrightarrow{u} = 0, \tag{3.2}$$

where $\overrightarrow{u}$ is the 3-D velocity vector, p is the kinematic pressure, and ν is the kinematic viscosity.

Applying the finite element method to the x and y momentum components and continuity equation, yields

$$\int_{\Omega} \phi_i \overrightarrow{U}_{cont} d\Omega + PSPG = 0 \tag{3.3}$$

$$\int_{\Omega} \phi_i \overrightarrow{U}_{mom} d\Omega + SUPG = 0 \tag{3.4}$$

where $\overrightarrow{U}$ represents the momentum and continuity equations and $PSPG$ and $SUPG$ are terms that couple the pressure terms and stabilize non-linear convective terms, respectively. The equations have been integrated over the entire domain, Ω, at each cell (i) and the basis function at each cell is indicated by ϕ. The formulation for this solver utilized linear 2-D triangular elements.

Recall that the discrete time accurate Fourier transformation of any scalar distribution can be written as

$$\hat{q}(x, y, t) = \sum_{k=0}^{N-1} q_n(x, y, t) e^{-\frac{2\pi I k}{N} k} \tag{3.5}$$

where $I = \sqrt{-1}$, N is the number of samples or modes in the set, and n is the Fourier mode index. The variable $\hat{q}$ represents the transformed scalar in Fourier space. The Fourier transformation of these equations yields a series of independent 2-D linear problems for each mode:

$$A_k \begin{bmatrix} \Delta\widehat{p}_k \\ \Delta\widehat{\overrightarrow{u}}_k \end{bmatrix} = \begin{bmatrix} \widehat{R}_{p,k} \\ \widehat{\overrightarrow{R}}_{u,k} \end{bmatrix} \tag{3.6}$$

where $\widehat{R}_{p,k}$ and $\widehat{\overrightarrow{R}}_{u,k}$ are the non linear terms and $A_k = M_1 + M_2(2\pi Ik/L) - M_3(2\pi k/L)^2$. The M terms are population matrices which are described in detail in Snyder and Degrez [19].

A variety of benefits stem from this method. First, decoupling of the linear solution for each Fourier mode lends well to computational parallelization. Second, each Fourier mode utilizes the same 2-D mesh to compute the spanwise velocity and pressure distribution at each mesh node. The spanwise-periodic 3-D flow field

is obtained after taking the inverse discrete Fourier transform. Third, a natural symmetry is present in the Fourier modes when considering the transform of a purely real scalar field. This means that computations are only required for half of the total number of modes.

Temporal discretization of the equations consists of a second order accurate explicit Adams-Bashforth method for the convective terms and a second order accurate Crank-Nicolson method for the diffusion and pressure terms. The use of an explicit scheme for the convective terms imposes a stability restriction on the time step. Lastly, signal aliasing in the Fourier transform is eliminated by only activating half of the total modes. The solver has been successfully validated against various classic fluid flows [19, 20, 21].

3.1.2 VGJ Boundary Condition

By nature of the hybrid method described above, the simulation of complex, fully three-dimensional shapes such as a wing or car is not readily tractable. Though significantly simpler, a hole is still a three-dimensional geometry whose boundary condition requires a different approach from Cartesian coordinate-system solvers. In light of the spectral method employed in this solver, the periodic spanwise placement of the VGJ holes in the experimental setup is crucial to creating such a boundary condition. It was developed such that for a given horizontal two-dimensional boundary, a single three-dimensional hole could be simulated in the spanwise direction, whose geometry is dictated by user-specified parameters read from a text file at solver initialization. Geometry-specific parameters consist of x and z location, horizontal radius, and vertical radius (for modeling ovals), all in units of meters. Non-geometric parameters consist of jet velocity magnitude, pitch angle, skew angle, pulse frequency, and duty cycle.

Implementation of the boundary condition is straight-forward and done by looping through each node on the VGJ boundary and setting a velocity distribution in the spanwise or z direction that is, in effect, one full period of a periodic step function. The step function at a given node is created by moving in real space

along the straight line extending in the spanwise direction from the boundary node, and assigning velocities depending on where the (x, z) coordinate lies in relation to the hole boundary, i.e. jet velocity if inside the hole and zero otherwise. This is performed for each velocity component. Each step function is then transformed to Fourier space and used to populate the solution matrix. Figure 3.1 shows the three

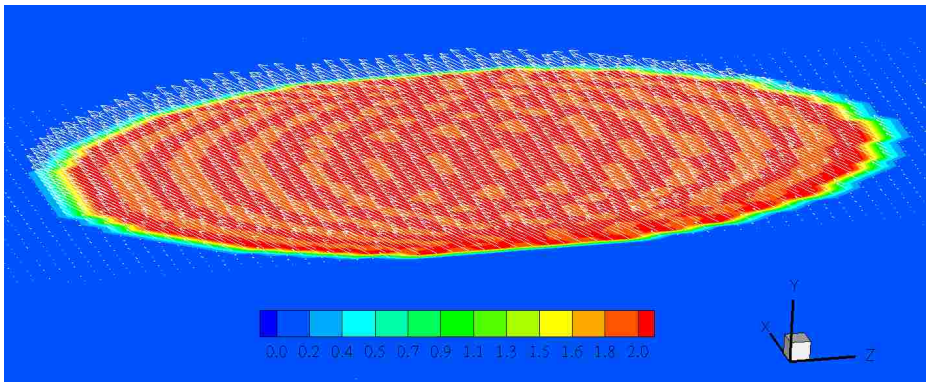

Figure 3.1: Contours of normalized velocity magnitude on VGJ boundary condition. Velocity vectors indicate direction of flow exiting hole.

dimensional boundary condition for the oval hole simulated in this study. Note the ripples in the velocity distribution resulting from the discrete Fourier representation of a step function. Though velocity profiles at the hole exit were obtained from the experiments, a step function was deemed sufficient for this work.

Pulsing parameters (frequency and duty cycle) were also factored into the boundary condition, based on the current time step and the assumption that pulsing begins from a flow time of zero seconds. As with the velocity exit profile, and as shown in Figure 2.4, the pulse cycle was approximated as a step function as opposed to using the experimental pulse profile.

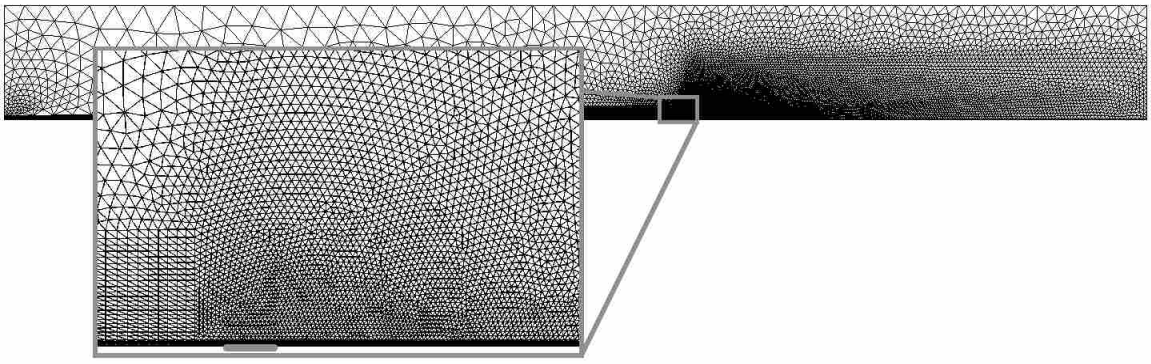

Figure 3.2: Coarse two-dimensional mesh used for initial ZPG cases. VGJ boundary condition indicated by short thick grey line on bottom wall in the zoom region.

3.2 Meshes

3.2.1 Zero Pressure Gradient

Figure 3.2 shows the coarse 2-D mesh used in initial ZPG calculations. All meshes were created in the commercial code GAMBIT. The computational domain retains the geometry scale of the experimental setup though the height was trimmed to y/d=15 and extends only 0.24 m aft of the VGJ. Boundary conditions were specified as follows: the vertical wall to the left was set to a Dirichlet velocity inlet, the top horizontal and right vertical boundaries were set to outflows and the bottom horizontal boundary to a no-slip wall. The bottom wall was split to create a small boundary segment $1d$ in length, centered at x=0.36 m, for the VGJ. The zoom region in Figure 3.2 shows the location of the VGJ boundary as indicated by the thick grey line slightly off center, along the bottom wall. A special boundary layer mesh was created upstream of the VGJ which, near the velocity inlet, is characterized by a very coarse resolution in the x direction but highly refined resolution in the y direction. This resulted in high aspect ratio cells near the wall at the inlet, which border a zone of very coarse cells filling the mid-passage domain. These boundary layer cells became more refined approaching the VGJ. This was done primarily to reduce the cell count and was justified in light of the fact that the boundary layer upstream of the VGJs for

both pressure gradient settings is laminar, thus focusing on the direction containing the steepest velocity gradients.

Table 3.1: Total cell count for four mesh resolutions.

Node resolution at VGJ (XY plane)	128 Fourier Modes	256 Fourier Modes
0.2 mm	3.5×10^6	7.0×10^6
0.15 mm	6.3×10^6	12.6×10^6
0.15 mm (wedge)	–	15.3×10^6
0.1 mm	–	15.6×10^6

The height of the refined region surrounding the VGJ was selected based on jet plume heights measured from the experiments. For all resolutions, the cells in this region grow smoothly until reaching the outlet boundary, having reached a characteristic length of 0.01 m. Mesh resolution was varied based on the node spacing along the VGJ hole boundary and on the total number of Fourier modes used in the spanwise direction. Total cell counts for the four meshes evaluated in this study (3 flat plate, 1 wedge) are shown in Table 3.1, for spanwise resolutions of 128 and 256 total Fourier modes.

3.2.2 Adverse Pressure Gradient

The experimental setup shown in Figure 2.2 was simulated by extending the domain of the medium resolution ZPG mesh described in Section 3.2.1 (indicated by the heavy black line spanning the domain in Figure 3.3) to include the entire wedge configuration. The geometric profile was obtained directly from the experimental apparatus. The mesh surrounding the VGJ was left unchanged. In addition, the channel domain was extended in the x direction to 1.2 m, with coarse cells and no boundary layer meshing (not shown). This extention was designated as a dissipation region for vortices emanating from the separation zone and was necessary because of solver instability when these vortices crossed the outflow boundary. In addition, a viscosity buffer was applied aft of x=0.9 m, which significantly reduced vortex strength

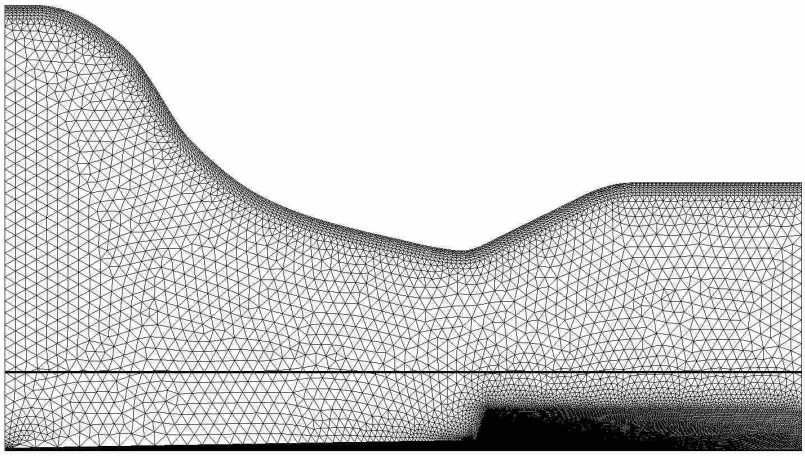

Figure 3.3: Two-dimensional mesh of wedge configuration. Heavy black line represents vertical extent from bottom wall of ZPG meshes.

prior to crossing the outflow boundary. This buffer was implemented by multiplying the molecular viscosity by a constant greater than one, to all cells downstream of the specified x location. No studies were performed to ascertain the influence on the upstream flow field resulting from this buffer, though they are believed to be negligible.

Most boundary conditions for the wedge configuration remained unchanged from the ZPG mesh, with the exception of the upper edge, which now consisted of the wedge wall and suction boundary. The suction boundary (Figure 2.2) was simulated with a Dirichlet velocity condition whose components were set such that the velocity magnitude was normal to the boundary and pointed away from the free stream. Verification of the C_p distribution was performed in the same manner as the experiments: by extracting the velocity profile along a line $15d$ above the VGJ plate. The C_p plot will be presented in Chapter 5 in conjunction with the numerical simulation results.

3.3 Mesh Resolution Study

3.3.1 Spanwise Resolution

A mesh resolution study was performed on the ZPG steady jet case to ascertain the level of refinement necessary for adequate resolution of the near-jet flow field. The differences between two Fourier resolutions will be discused first. All line plots in this section were extracted along lines at the intersection of the horizontal plane at y/d=1.5 and various x/d planes perpendicular to the free stream, moving downstream of the jet. The jet fluid exits from x/d=0 and z/d=8.5, in the negative spanwise direction.

Figure 3.4 plots streamwise vorticity from the medium resolution mesh comparing 128 and 256 total Fourier modes. Variations in the vorticity distributions between the two resolutions are visible, and were deemed sufficiently large to justify the use of the increased spanwise resolution in all simulations. The simulations were limited to 256 modes in light of computational resource restrictions.

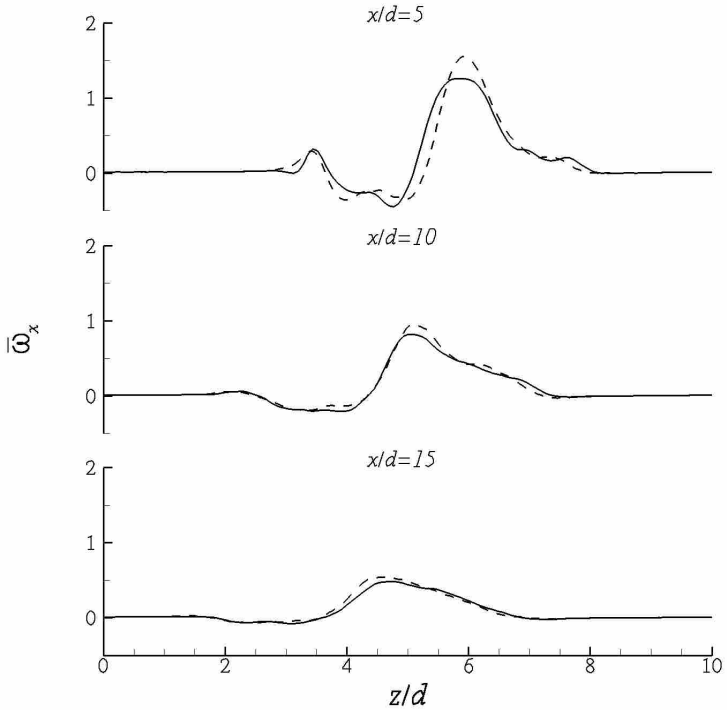

Figure 3.4: Spanwise grid resolution study of streamwise vorticity, $\overline{\omega}_x d/U_\infty$, at various x/d locations. $-$ 128 Fourier modes, $--$ 256 Fourier modes.

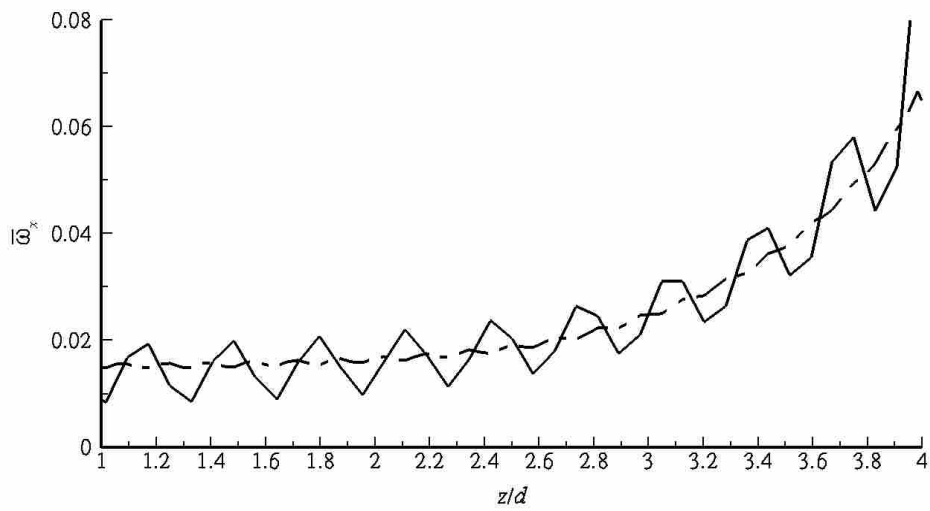

Figure 3.5: Spanwise grid resolution study of streamwise vorticity, $\overline{\omega}_x d/U_\infty$, for coarse mesh at x/d=1. $-$ 128 Fourier modes, $--$ 256 Fourier modes.

Figure 3.5 shows a section of the flow field to the left of the jet fluid zone at x/d=1 and y/d=1.5. Of note are the oscillations in the vorticity distribution, particularly noticeable in the 128 mode curve. This phenomenon is a residual of the discrete Fourier approximation of the velocity field around the jet structure which, at each node, is effectively a spanwise step function. Though it is clear that increasing the spanwise resolution minimizes these oscillations, they can never be fully eliminated and occasionally appear in other plots in this study. Their magnitudes are clearly reduced when increasing the resolution to 256 modes but are never fully eliminated.

The precise measure of the fluctuations is difficult, but are of highest magnitude in the region directly surrounding the hole. Identical fluctuations are found along the wall on the VGJ boundary condition in the spanwise direction. Velocity magnitude variation along this boundary was observed at $\pm$1.4% of the free stream velocity. It should also be noted that the fluctuations do not propagate downstream and are simply the residual of the numerical method, much like the "smearing" effect visible in a second-order finite difference approximation of a step function.

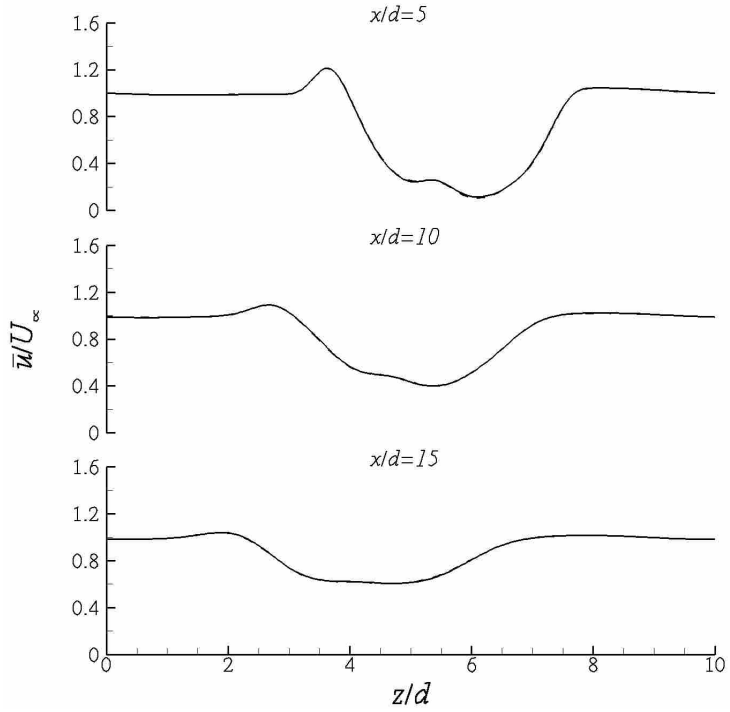

Figure 3.6: Time averaging comparison for streamwise velocity, $\overline{u}/U_\infty$, for 400k and 600k time steps. − 400k time steps, −− 600k time steps.

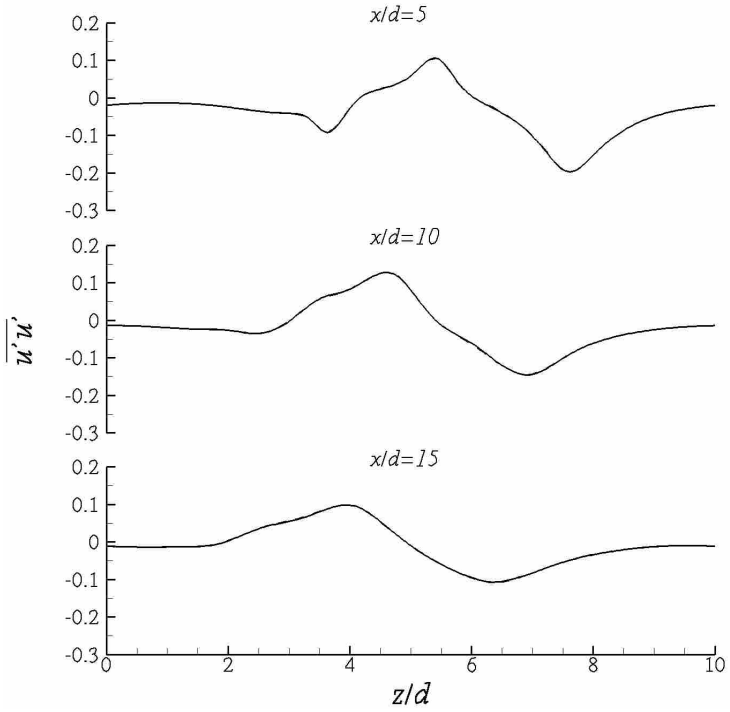

Figure 3.7: Time averaging comparison for Reynolds stress, $\overline{u'v'}/U_\infty^2$, for 400k and 600k time steps. − 400k time steps, −− 600k time steps.

3.3.2 Time Averaging

In the steady ZPG case, a time average study was performed evaluate how many time steps were necessary for sufficiently averaged flow fields. Figures 3.6 - 3.8 show the results of time averaging the medium resolution mesh over 400,000 and 600,000 time steps. For this mesh, a time step of 2×10^{-5} s was used, which resulted in a total flow time of 8 s. This time step magnitude resides at the upper limit at which solver stability is maintained. It was observed that increasing the time averaging by 200,000 time steps (4 s) negligibly changes the flow field any location in the domain, regardless of the flow variable. Thus, all time-averaged plots in this study were calculated over 8 seconds of flow time.

3.3.3 XY Plane Resolution

A study was performed on the three xy plane resolutions averaged over 400,000 time steps for 256 Fourier modes. Flow structures and turbulent statistics were compared for each resolution. For the coarse and medium resolution meshes, a time step of 2×10^{-5} s was used. This resulted in a maximum CFL number of 0.4 and 0.6 respectively. The jet is not factored into the CFL number because the velocity magnitude points primarily in the spanwise direction, where instabilities of this type chiefly occur in the xy plane. In the case of the fine mesh, a time step of 1×10^{-5} s was required in order to ensure solver stability. This resulted in a CFL number of 0.4 without the jet. The reduced time step for this mesh required 800,000 time steps to match the equivalent flow time of the other meshes.

The non-dimensional boundary layer parameter y^+, defined as

$$y^+ = \sqrt{\frac{du/dy}{\nu}}y, \tag{3.7}$$

where du/dy is the velocity gradient at the wall and y is the normal distance of the first node off the wall, was calculated for the medium and fine meshes along the flat plate approaching the VGJ. Maximum values of 2.3 and 0.5 just upstream of the jet, were calculated for each mesh respectively. This indicates that, in the absence of wall

functions to model boundary layer characteristics, this mesh is sufficiently resolved in the near wall region by remaining within the limits of proper mesh resolution ($y^+ = 1 \rightarrow 2$).

Figures 3.9 - 3.12 plot the spanwise distributions of streamwise velocity component, Reynolds stress, streamwise vorticity, and streamwise velocity gradient in the wall normal direction. With the exception of the velocity gradient (Figure 3.12), all meshes are similar in resolving the flow field at x/d=15. Closer to the jet however, at x/d=5 and 10, it is clear that the medium and fine resolution meshes resolve flow features not calculated by the coarse mesh. This can be noted in trends and magnitudes of peaks and troughs in the plots. Though minor differences do exist between the medium and fine meshes, they are mostly present in magnitude variations, as opposed to flow structure formation. As such, the fine mesh was chosen for the steady ZPG simulation, and the medium mesh for the ZPG and APG pulsed simulations. The medium resolution mesh was confidently chosen (based on the above analysis) for the pulsed cases primarily because of computational resource limits.

3.4 Viscous Model Selection

Directly linked to the grid resolution study is the decision to forgo the use of a turbulence model, in this case LES, for these simulations. The primary concern in simulating turbulence without a model is the importance of a sufficiently refined mesh and time step such that all turbulent length and time scales are accounted for. On the other hand, LES operates on the assumption that below a certain energy level, the smallest turbulent fluctuations are identical from flow to flow and can be modeled, while the large eddies are resolved by the mesh and time step. Both methods are restricted to low Reynolds number flows. The decision not to use LES was based on the following.

First, while the Reynolds number (based on plate length) of these simulations is approximately 50,000, it reduces to 1,100 when based on hole diameter and jet velocity. This is historically categorized as being within the range of a feasible simulation without a turbulence model. Furthermore, the only region of turbulence in the

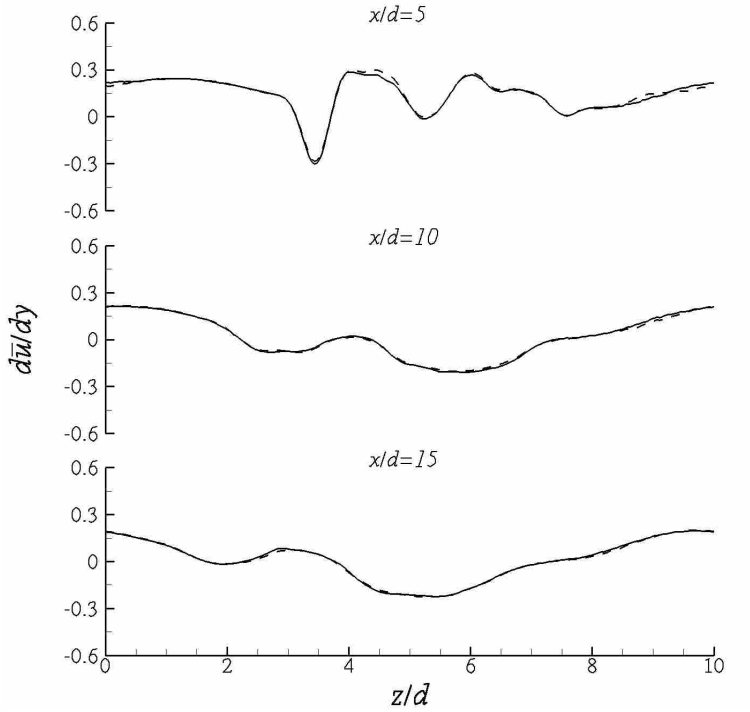

Figure 3.8: Time averaging comparison for streamwise velocity gradient, $d\overline{u}/dy$, for 400k and 600k time steps. $-$ 400k time steps, $--$ 600k time steps.

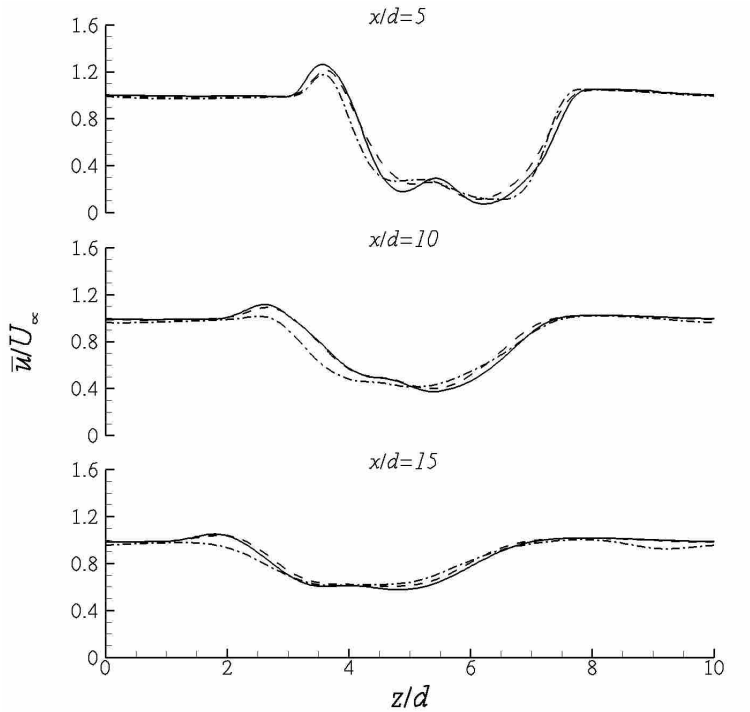

Figure 3.9: Grid resolution study in xy plane for streamwise velocity component, $\overline{u}/U_\infty$, at various x/d locations. $-$ Fine mesh, $--$ medium mesh, $-\cdot-$ coarse mesh.

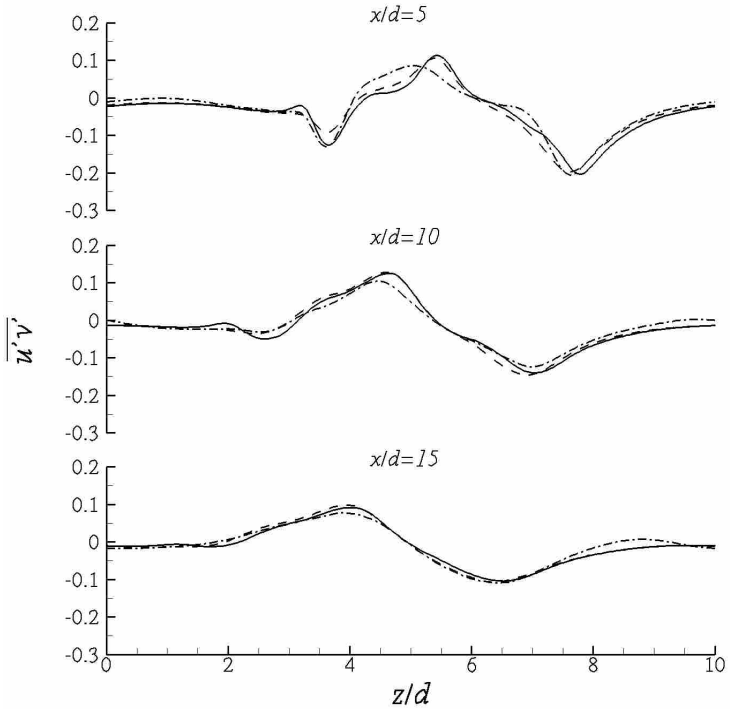

Figure 3.10: Grid resolution study in xy plane for Reynolds stress, $\overline{u'v'}/U_\infty^2$, at various x/d locations. $-$ Fine mesh, $--$ medium mesh, $- \cdot -$ coarse mesh.

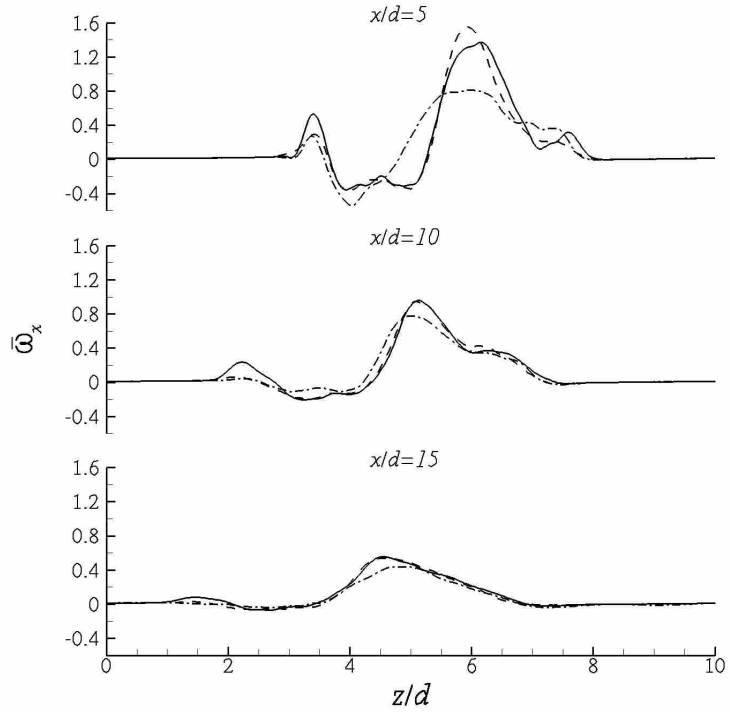

Figure 3.11: Grid resolution study in xy plane for streamwise vorticity, $\overline{\omega}_x d/U_\infty$, at various x/d locations. $-$ Fine mesh, $--$ medium mesh, $- \cdot -$ coarse mesh.

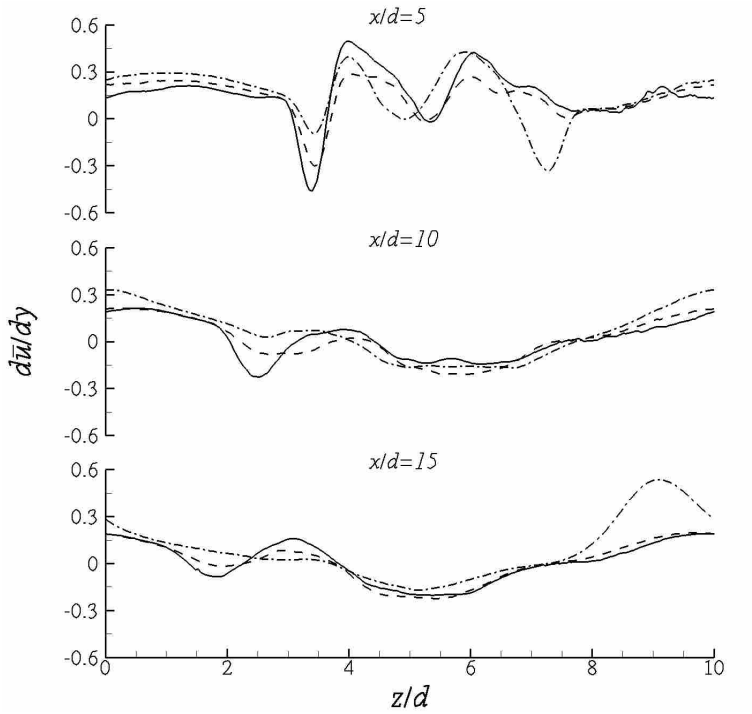

Figure 3.12: Grid resolution study in xy plane for streamwise velocity gradient, $d\overline{u}/dy$, at various x/d locations. $-$ Fine mesh, $--$ medium mesh, $- \cdot -$ coarse mesh.

domain lies in the jet wake. The predominantly laminar flow field meant cells could be safely grouped at the hole and near-jet wake. Thus, in regions where LES would be needed, a very high mesh resolution was already utilized.

Second, the LES model used in this solver employs a dynamic turbulent viscosity. This means that a turbulent viscosity is applied at each cell based on the cell size and local strain rate tensor. In this manner, the turbulent viscosity is only applied at cells that are experiencing large velocity gradients or turbulent fluctuations. For the medium and fine meshes, the maximum ratio of turbulent viscosity to molecular viscosity inside the jet wake was observed at less than 9% and 7.5% respectively. Furthermore, these values are isolated peaks occurring downstream of the VGJ in coarse regions (large cells) of the wake, and largely outside the regions of interest. Most of the jet wake contained ratios of 3% or less at both resolutions. This would correspond to a 3% cell-localized change in Reynolds number after the

application of the turbulent viscosity. Such a change was not deemed large enough to justify the use of a turbulence model.

Chapter 4

Zero Pressure Gradient

4.1 No Control

Before considering the effects of the VGJ, a laminar boundary layer with no jet actuation was analyzed. Figure 4.1 shows the computational mesh superimposed over contours of normalized streamwise velocity, showing the scale of the mesh resolution in relation to the boundary layer height and hole diameter. These dimensions are indicated by the thick white line extending from the y/d axis on the left and the short white line along the bottom wall at x/d=0. Mesh details can be found in Section 3.2.1.

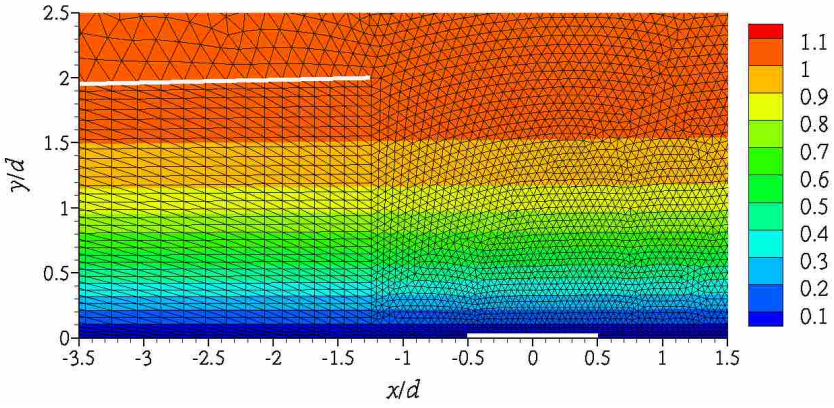

Figure 4.1: Contours of average streamwise velocity, $\overline{u}/U_\infty$, showing no-control laminar boundary layer in ZPG. The white line extending horizontally from y/d axis represents the vertical extent of the custom boundary layer mesh. The short white line on the bottom wall represents the VGJ boundary.

The boundary layer profile at the jets is shown in Figure 4.2, plotted against the Blasius solution for this Reynolds number. Reynolds number based on momentum

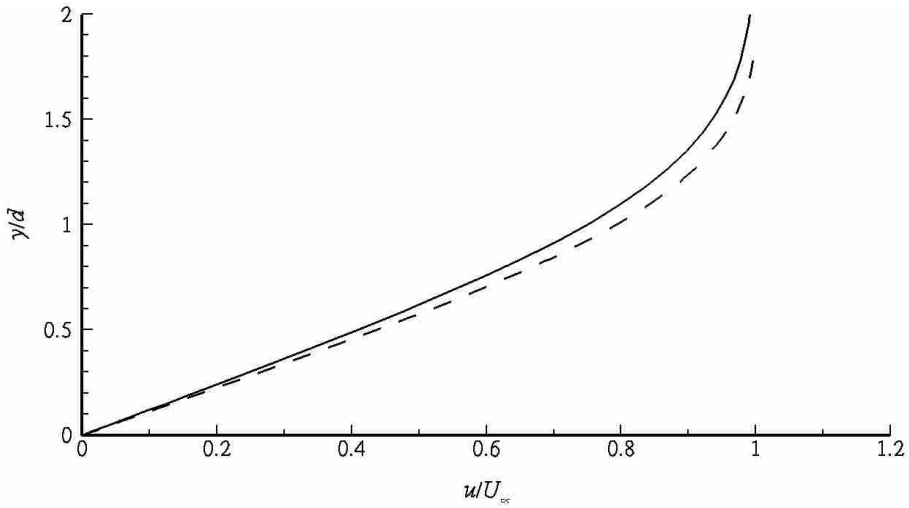

Figure 4.2: No-control laminar boundary layer profile in ZPG at VGJ, plotted with Blasius solution. − Blasius, −− numerical.

thickness was calculated at 135 which is a difference of 11% from the experimental value of 150. The primary reason for calculating this value is to ensure that the boundary layer is below the critical Reynolds number of 200, at which unsteady fluctuations no longer dissipate.

4.2 Steady Jet

After enabling the VGJ (B=2) for the fine mesh and allowing the simulation to reach a statistical steady state, the flow field was time averaged over 800,000 time steps at $\Delta t = 1 \times 10^{-5}$ s. This yielded a maximum CFL of 0.4, not factoring in the VGJ and equated to 8 s of flow time. Each time step required approximately 2 s of processor time which resulted in a total of 18 days running on 64 processors of a Dell 1955 Linux Cluster.

Figures 4.3 - 4.5 show spanwise plots located at the intersections of the y/d=1.5 plane and various x/d planes downstream of the jet. The y/d=1.5 position was chosen because it vertically splits the jet fluid convecting downstream of the hole. The VGJ exits the xz plane at x/d=0 and z/d=8.5, in the negative spanwise direction. Overall, the plots show very good agreement with the experimental trends. It is clear from all three figures that the wake has drifted slightly more in the spanwise

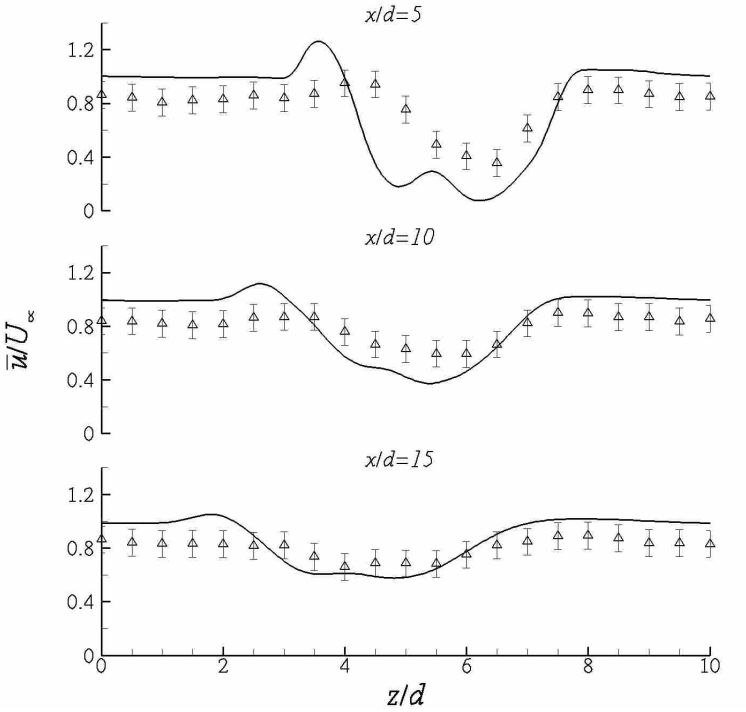

Figure 4.3: Comparison of average experimental and numerical streamwise velocity, $\overline{u}/U_\infty$, at various x/d locations. $\triangle$ Experiment, $-$ fine mesh.

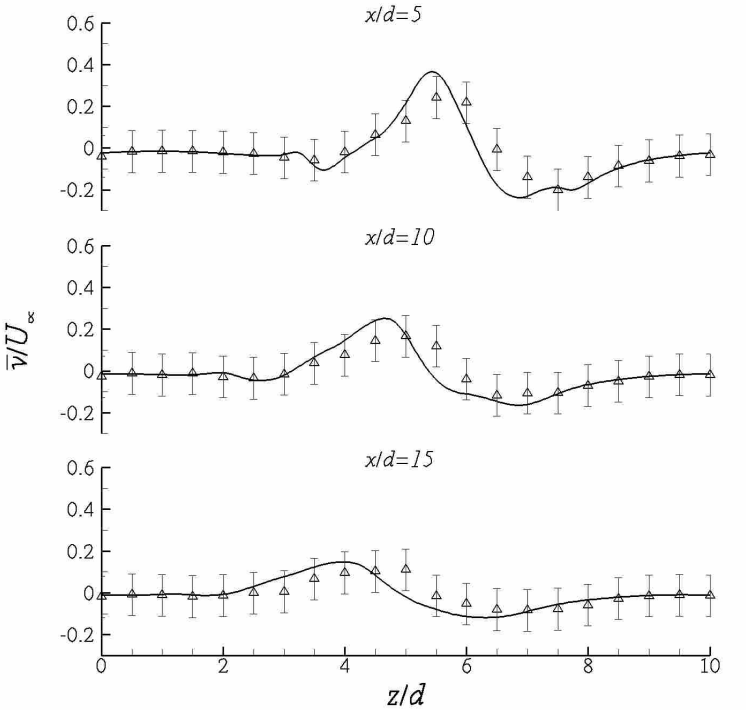

Figure 4.4: Comparison of average experimental and numerical wall-normal velocity, $\overline{v}/U_\infty$, at various x/d locations. $\triangle$ Experiment, $-$ fine mesh.

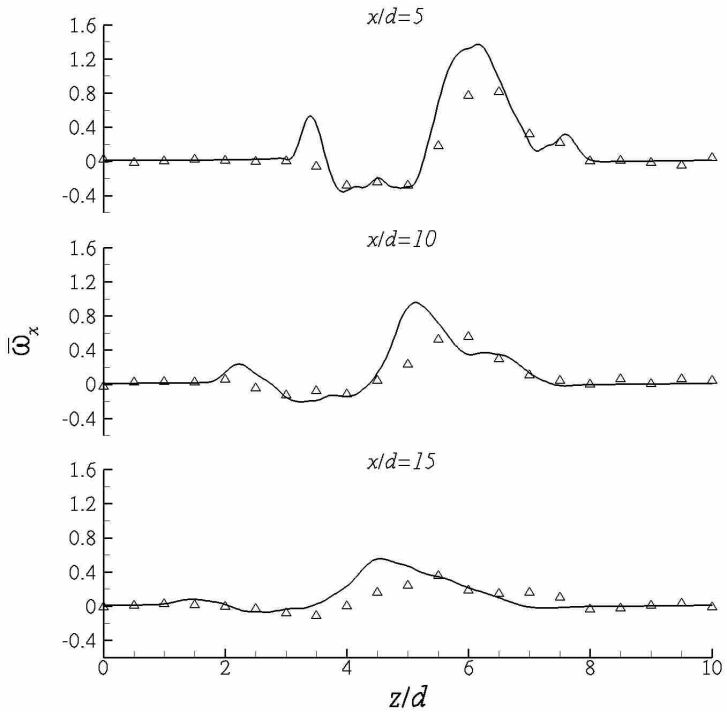

Figure 4.5: Comparison of average experimental and numerical streamwise vorticity, $\overline{\omega}_x d/U_\infty$, at various x/d locations. $\triangle$ Experiment, $-$ fine mesh.

direction and the wake magnitudes dissipate slower, in the numerical simulations. Also readily apparent are differences due to resolution. As discussed in Chapter 2, the experimental spanwise resolution was set to 2 mm, or $0.5d$ whereas it is $0.04d$ in the numerical simulations. Though the differences are visible in all plots, it is particularly apparent in streamwise vorticity calculations which utilize a finite difference in the spanwise direction. This finite difference over the relatively high experimental Δz, minimizes flow features in the near-jet region and can result in slightly lower scalar magnitudes.

There is a well defined streamwise momentum deficit at all x/d locations in Figure 4.3 which is caused by the jet fluid blocking the free stream. It also corresponds with fluctuations in streamwise vorticity at the same z/d locations. The large peak of positive vorticity indicates the presence of a clockwise rotating vortex which increases in size and decreases in strength, moving downstream. To the left of this positive peak, there is a weak negative region of vorticity. This represents the remains of a

secondary, counter-clockwise rotating vortex whose core has been enveloped by the primary vortex at these x/d locations. The presence of a vortex is also confirmed with an inflection point in the wall-normal velocity (Figure 4.4) plot. This trend represents upwash and downwash components of the clockwise rotation.

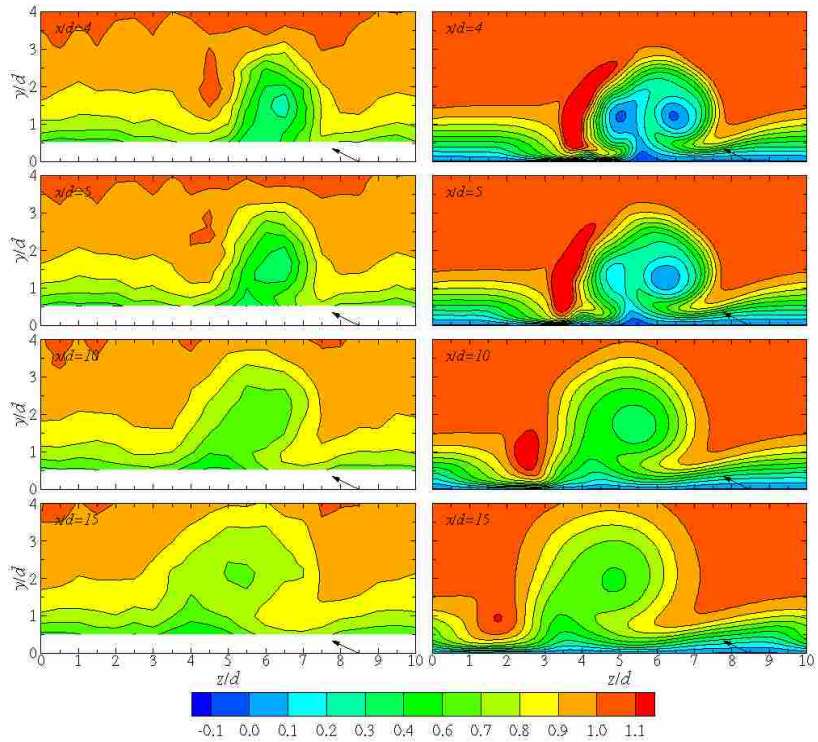

Figure 4.6: Contours of average experimental and numerical streamwise velocity, $\overline{u}/U_{\text{inf}}$, at various x/d planes. Experiment in left column.

Figures 4.6 - 4.8 consist of contour plots on planes normal to the free stream flow of both the experimental and numerical flow fields, at various x/d locations. In all plots, arrows pointing to the left at an angle, from x/d=8.5, indicate the location and direction of the VGJ. These figures show excellent agreement with the experiments. The general shape (Figure 4.6) of the low streamwise momentum region is matched very well by the numerics. As the jet convects downstream, it develops into a lobe which tucks underneath itself to the right and slightly thickens to the left. These regions indicate the mixing of low momentum boundary layer fluid (left) and high

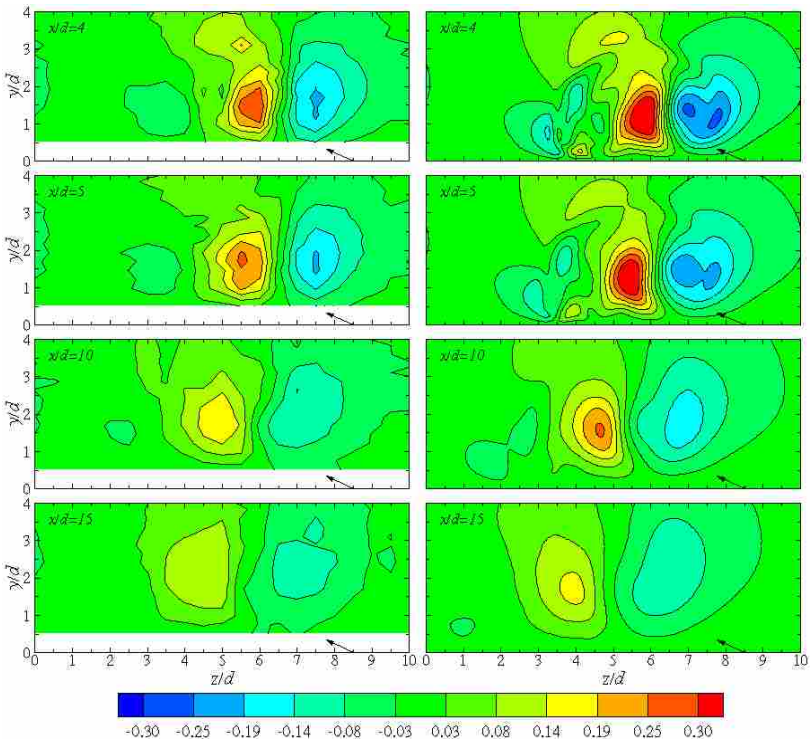

Figure 4.7: Contours of average experimental and numerical wall-normal velocity, $\overline{v}/U_{\text{inf}}$, at various x/d planes. Experiment in left column.

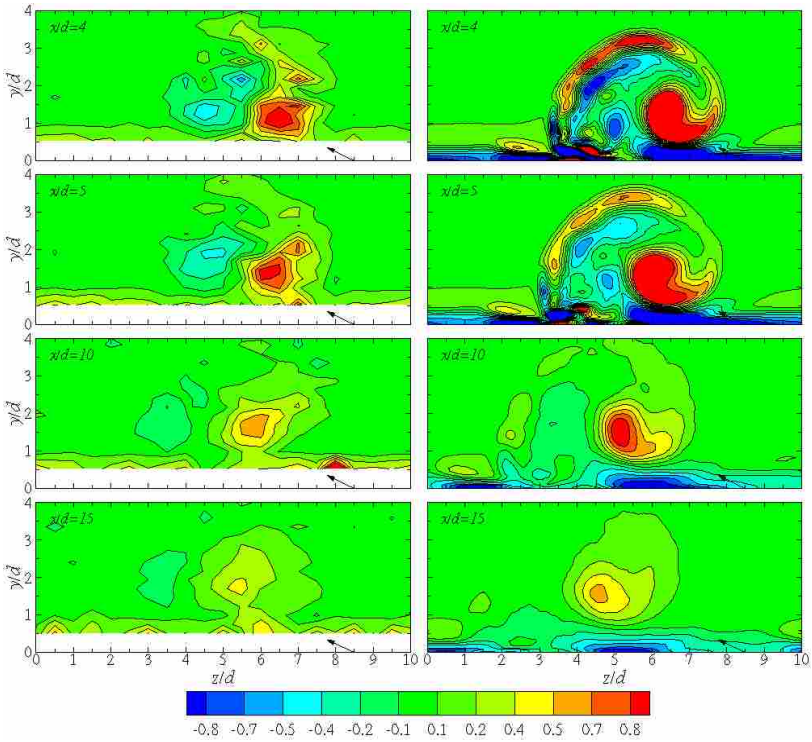

Figure 4.8: Contours of average experimental and numerical streamwise vorticity, $\overline{\omega}_x d/U_\infty$, at various x/d planes. Experiment in left column.

momentum free stream fluid (right). Absent from the experiments however, is a sharp trough of high velocity fluid to the left of the primary structure (x/d=10,15 , $z/d \approx$2). This trough will be discussed in the following section. The wall normal velocity (Figure 4.7) is well resolved, clearly showing the upwash (left side) and downwash (right side) regions of the vortex.

Figure 4.7 offers another view of the upwash and downwash regions of the flow field with contour plots of normalized wall-normal velocity. The unstructured flow features centered at z/d=4 and x/d=4,5 are visible in both columns and magnitudes of each region agree well. They dissipate quickly as the primary vortex grows in size.

The shape and magnitude of streamwise vortical structures (Figure 4.8) also compares very well. The primary vortex is clearly visible in all x/d planes. The vortex accurately dissipates and expands as it travels downstream. The remains of the secondary vortex is also present in both plots, to the left of the primary vortex core. Of note in these plots is the accurate simulation of a thin, circular wall region extending from the downwash side of the vortex and arching around the top, to a height of $\sim$3.5d at x/d=5.

Wall-normal and streamwise vorticity on the y/d=1.5 plane are shown in Figures 4.9 and 4.10, where the VGJ hole is indicated by the oval located at x/d=0 and z/d=8.5 and the free stream is moving in the positive x/d direction. Viewer perspective is looking down on the VGJ. Though barely discernable in the experiments, the presence of a strong positive vorticity region wrapping around the leading edge of the jet fluid, followed by a thin negative region is clearly visible. These regions do not represent defined vortical structures as observed with the primary vortex shown in Figure 4.10, but indicate the passage region the core jet fluid. Also present in both vorticity plots is the weaker secondary vortex, directly above the positive vortex. The slight increase in spanwise drift of the VGJ wake is also discernable in the numerics.

Figure 4.11 shows time-averaged iso-surfaces of streamwise velocity for the experimental and numerical flow fields, colored with the wall normal velocity component. This surface surrounds the low momentum lobe of the primary vortex and the tucking to the right of the lobe near the wall is clearly visible. Vortex dissipation is

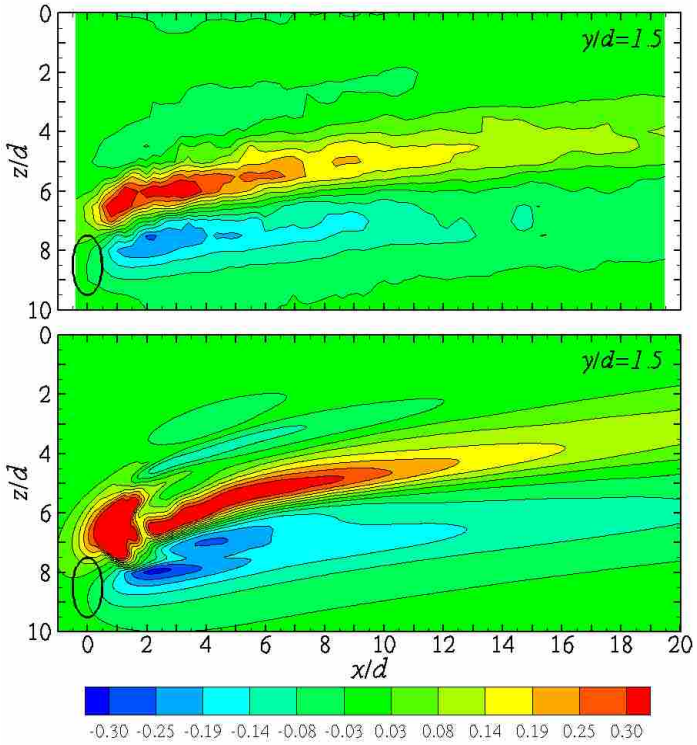

Figure 4.9: Contours of average experimental and numerical wall-normal velocity, $\overline{v}/U_{\text{inf}}$, at y/d=1.5. Perspective looking down on jet. Experiment in top plot.

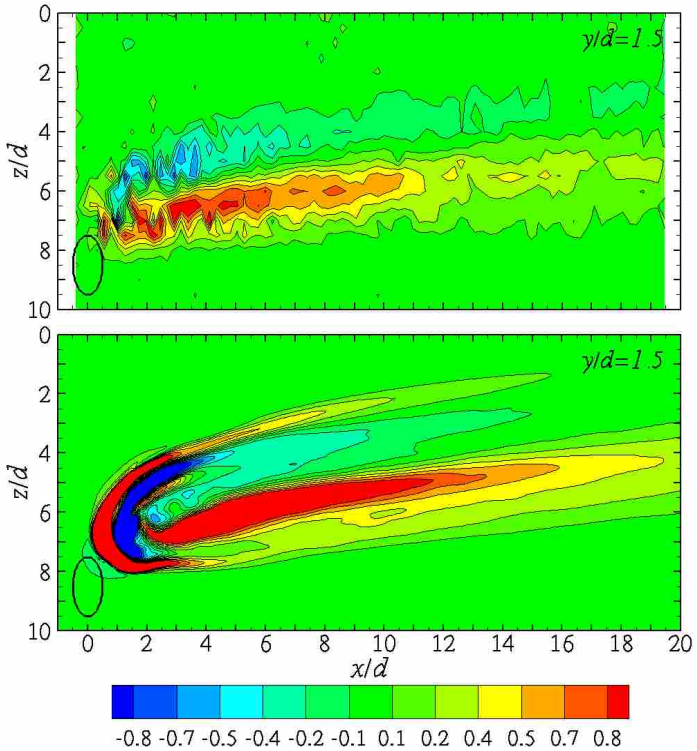

Figure 4.10: Contours of average experimental and numerical streamwise vorticity, $\overline{\omega}_x d/U_\infty$, at y/d=1.5. Experiment in top plot.

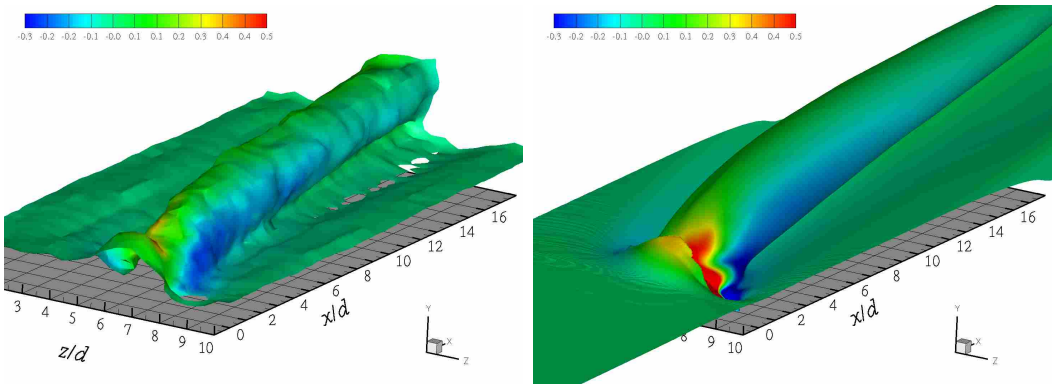

(a) (b)

Figure 4.11: Comparison of average experimental and numerical time-averaged iso-surfaces of streamwise velocity, $\overline{u}/U_\infty$=0.75. Experiment (a), numeric (b).

noted by the shrinking of the surface as it extends downstream as well as the fading of the wall normal velocity on the right side of the lobe. The lip on the leading edge of the jet fluid, just ahead of the primary vortex, is due to the free stream moving around the jet. The discontinuity in the surface at this location indicates the presence of the jet fluid, which has no streamwise component. The surface then continues on as the vortex is entrained by the free stream.

4.3 Steady Jet Numerical Analysis

The contour plots displayed previously show excellent agreement between the experiments and the numerical model. A more in depth analysis of the numerical simulations will be presented here. Figure 4.12 shows the pressure distribution at x/d=2. As expected, the vortex region is dominated by a low pressure zone. Also denoted in this and all of the following x/d plots, are the locations of the primary and secondary vortex centers, as indicated by the white and black circles respectively. These centers were extracted from velocity vector plots at each x/d location (not shown). Figures 4.13 - 4.14 show the time averaged VGJ flow field with the top plotting plane shifted closer to the jet (x/d=2). The contour limits have been adjusted to levels better suited to the magnitudes achieved in the numerics.

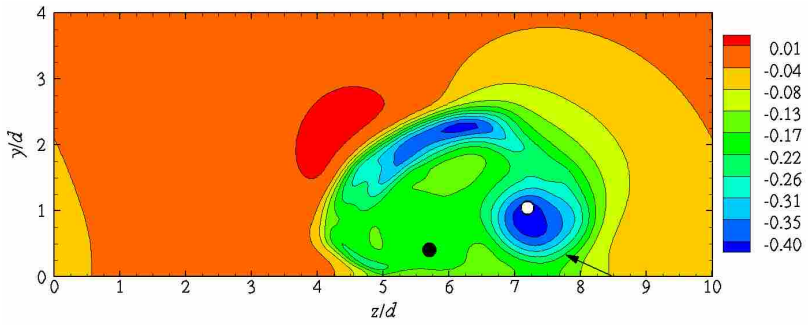

Figure 4.12: Contour plot of average numerical pressure at x/d =2.

Recalling the weak negative vortical structure in Figure 4.10 and noting the lack of secondary vortex markers downstream of the x/d=2 position, it is clear that the secondary vortex dissipates quickly. The brief presence of the secondary vortex and its rapid decay seem to coincide with two distinct regions of the VGJ wake. A formation region, where the primary vortex is developing and consumes neighboring structures, and a fully developed region, where the primary vortex dominates the flow field. The transition appears to occur around the x/d=5 location, which is not much further downstream from the dissipation point of the secondary vortex core, at approximately x/d=3.

The left column of Figure 4.13 plots the streamwise velocity component. The increase in streamwise velocity to the left of the primary vortex lobe was observed experimentally by Eldredge [18]. This could be the result of free stream fluid accelerating around the jet fluid (effectively acting as a solid obstacle), much like flow around an airfoil. It is also possible that the vortex slightly accelerates the fluid as it is pulled around the top of the lobe outer edge in the clockwise direction. The wall-normal velocity component does not show any significant changes, and well defined trends do not appear until the primary vortex has finished developing.

The left column of Figure 4.14 shows contours of the streamwise velocity gradient in the wall-normal direction. The vertical extent of the boundary layer fluid can be seen at x/d=2 represented by the contours extending horizontally from the y/d axis between 1.5 and 2. This height is consistent with Figure 4.2 which was taken from the no control case. As the primary vortex convects downstream, it contin-

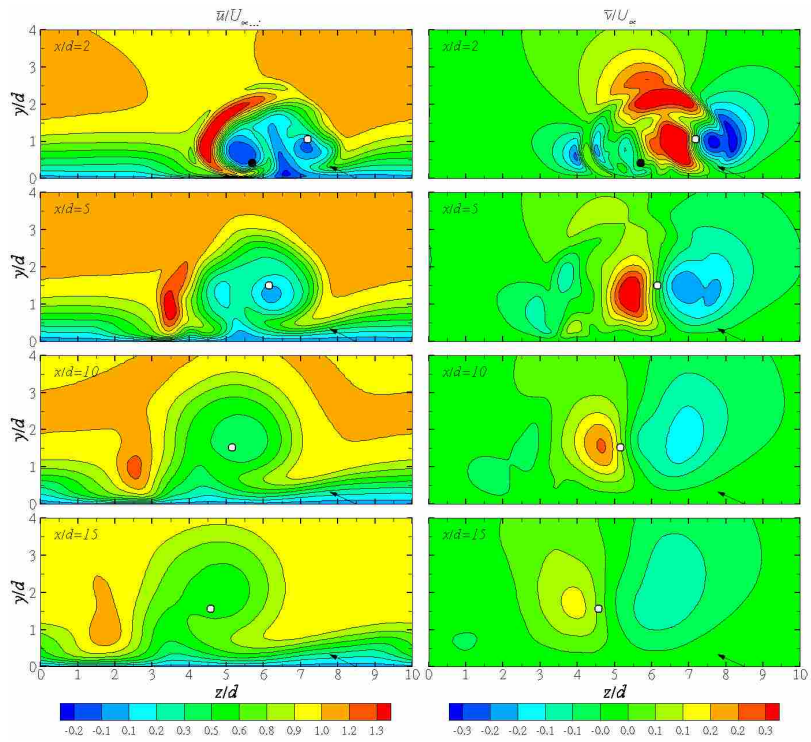

Figure 4.13: Contour plots of average numerical streamwise, $\overline{u}/U_\infty$ (left column), and wall-normal, $\overline{v}/U_\infty$ (right column), velocity at various x/d planes downstream of VGJ.

ues to carve the boundary layer as it spreads. Upon reaching the x/d=15 location, the boundary layer has been significantly reduced in size as the vortex influence has spread over most of the span width. A region of boundary layer remains to the right of the core but is greatly distorted by the vortex and just barely reaches its original height on the right side of the plot. The boundary layer structure described here contrasts with experiments conduced by Khan and Johnston [5] who measured the VGJ flow field at a Reynolds number based on the jet of 5,000, and 1,100 when based on momentum thickness. They reported a reduction in boundary layer thickness on the downwash side and a thickening on the upwash side, though streamwise velocity lobe shape was very similar.

Streamwise vorticity in the right column in Figure 4.14 at x/d=2 shows various structures surrounding the secondary vortex before being enveloped by the primary vortex. None of these features appear to have any significant effect on the flow field.

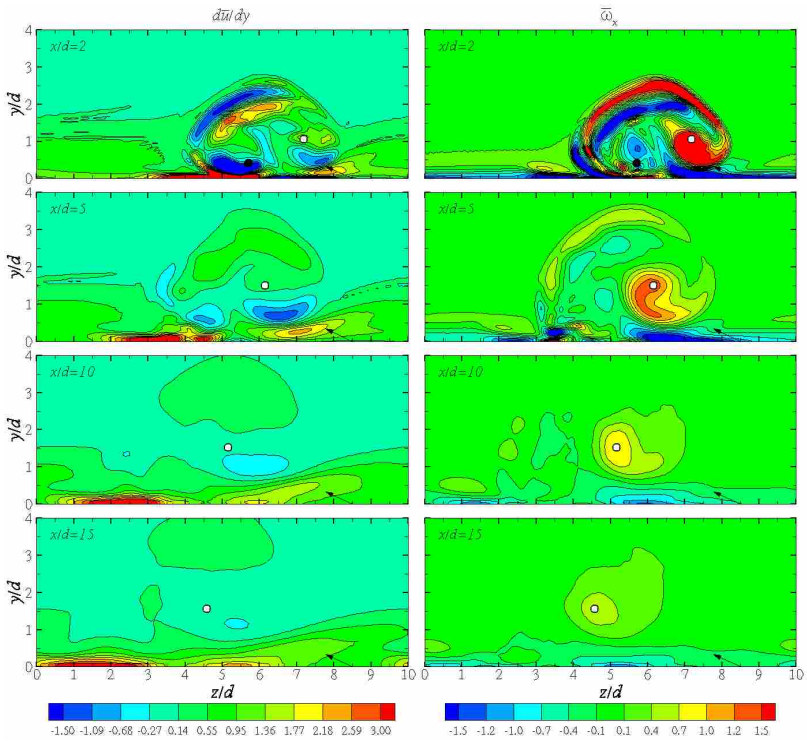

Figure 4.14: Contour plots of average numerical streamwise velocity gradient, $d\overline{u}/dy$ (left column), and streamwise vorticity, $\overline{\omega}_x d/U_\infty$, (right column) at various x/d planes.

Downstream of this point the vortex structure is largely identical to that in Figure 4.10.

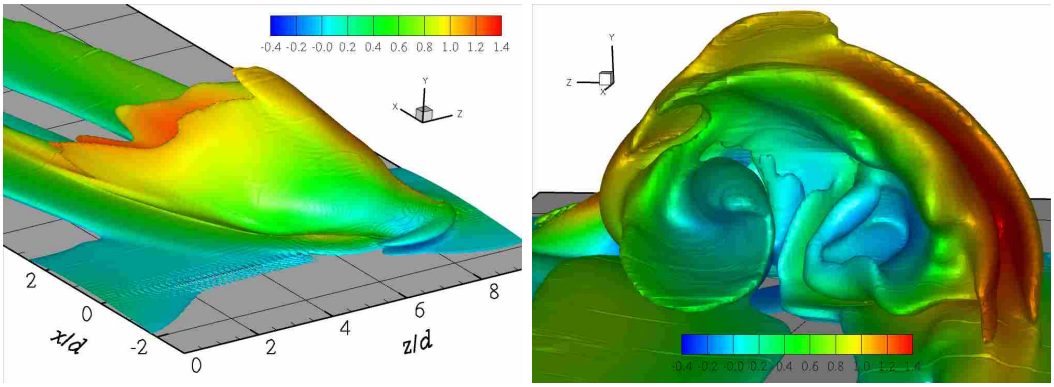

(a) (b)

Figure 4.15: Time-averaged numerical iso-surfaces of $\overline{\omega}_{mag} d/U_\infty$=1.5 colored by streamwise velocity. Perspective looking downstream (a), upstream (b).

Figure 4.15 shows iso-surfaces of vorticity magnitude colored with streamwise velocity, from two different perspectives. Looking downstream, the jet fluid is clearly visible exiting from xz plane and is smoothly entrained by the free stream. Looking upstream offers a very different view of the flow field. The primary (left of plot center) and secondary (right of plot center) vortices are seen curling up inside a shell structure surrounding the jet wake. Visible in the coloring is the streamwise velocity deceleration region in the vortex cores and the acceleration around the jet fluid in the shell wall.

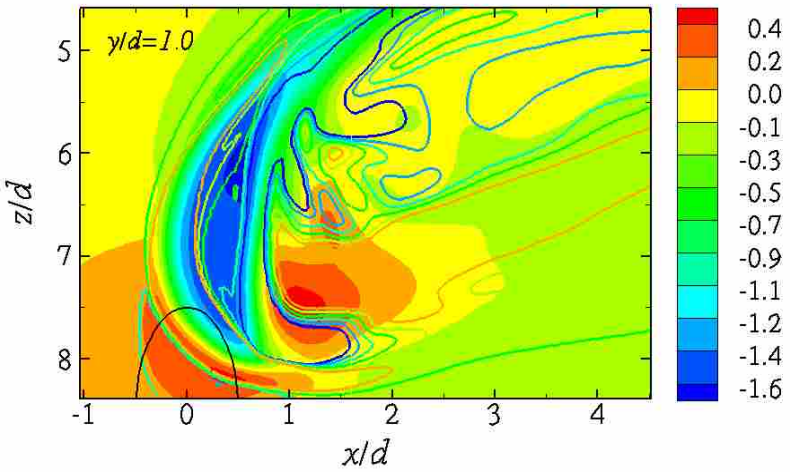

Figure 4.16: Contour plot of average numerical spanwise velocity, $\overline{w}/U_\infty$ at y/d =1.0, overlaid with lines of streamwise vorticity. Perspective is looking down on jet.

This perspective also shows two layers of equal vorticity magnitude forming the shell wall. The region between these layers contains the highest streamwise vorticity found in the domain, with the exception of the primary vortex core. This region also corresponds to the mostly irrotational flow of the core jet fluid. This is better observed by slicing the domain at y/d=1.0 and moving closer to the wall. Figure 4.16 shows a contour plot of normalized spanwise velocity overlaid with contour lines of streamwise vorticity. The vorticity lines are similar in coloring to Figure 4.8, with orange and blue lines surrounding regions of positive and negative vorticity, respectively. The

highly negative spanwise velocity (blue) in the plot is flanked by these opposite sign vorticity regions. The jet fluid exiting the hole has minimal vortical component. Vorticity regions surrounding this core fluid expand quickly as the fluid is curved in the direction of the free stream. At y/d=1.5 most of the jet core is mixed into the free stream (Figure 4.8).

This shell structure appears to initially provide a covering for the vortical structures forming inside. The vorticity of this shell wall (clockwise, from Figure 4.14) indicates it is rotating in the same direction as the primary vortex. The shell is sufficiently large to enclose both vortical structures. The proximity of the secondary vortex and the apparent lack of interaction with the shell wall would indicate that it is a product of the primary vortex roll-up as opposed to the direct influence of the jet fluid.

The shell wall also contains the highest turbulence levels in the domain, as shown in Figures 4.17 and 4.18. These plots clearly show laminar flow surrounding the turbulent region induced by the vortex. The growth of these regions is similar to that seen in the streamwise velocity plots.

Also of note in Figure 4.15(a) is the presence of a small spanwise vortical structure just in front of the jet fluid near the wall. This structure forms as the boundary layer fluid stagnates at the exiting fluid column, much the same way a horseshoe vortex typically forms at the base of a turbine blade near the hub wall. There is no indication the vortex wraps around the jet fluid.

4.4 Pulsed Jet

The frequency for pulsing in the ZPG case, based on Eq. 2.2, was set to 2 Hz at a duty cycle of 25%. Identical to the experiments, 40 flow fields were averaged at each of the eight phases shown in Figure 2.4. The pulsing case was conducted at B=2.5 and pulsing was initialized from the uncontrolled state described in Section 4.1.

A total of 1 million time steps were required to obtain 40 full pulses at this frequency. Because of the computational resources required for such large number of

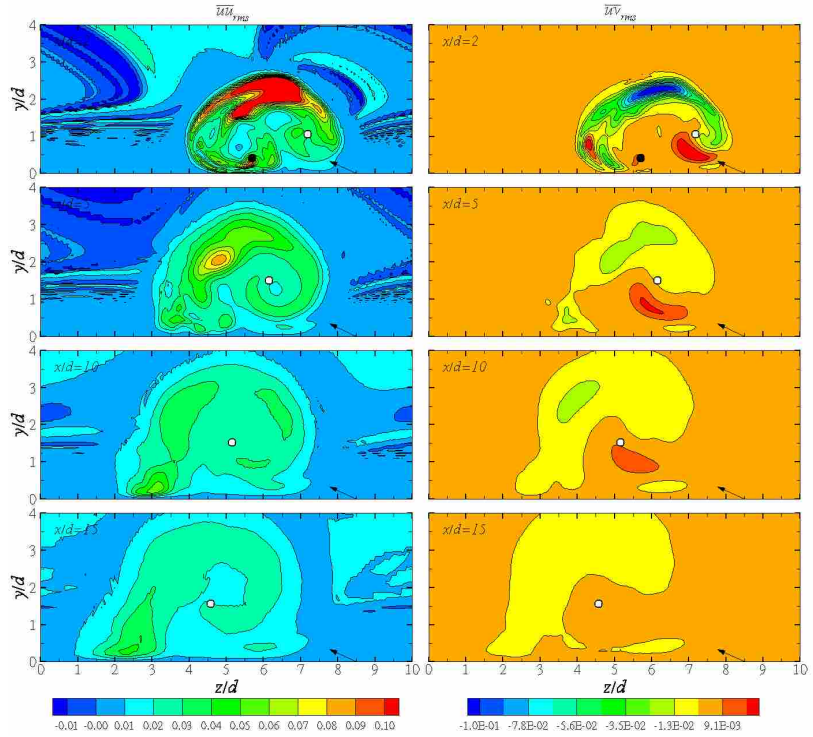

Figure 4.17: Contour plots of average numerical turbulence statistics, $\overline{uu}_{rms}/U_\infty^2$ (left column), and $\overline{uv}_{rms}/U_\infty^2$ (right column), at various x/d planes.

time steps, the medium resolution mesh was chosen based on its successful resolution of most of the flow features observed in the fine mesh, as discussed in Section 3.3. The solver averaged approximately 1.7 seconds to calculate each time step on 64 processors, which resulted in 20 days of computation time. SFELES was configured to extract instantaneous 3-D flow fields at intervals coinciding with the phase locations during each pulse; uncompressed, each file occupied 2.4 gigabytes of disk space. A Matlab script was written to parse the data files for a given phase and return a single file containing the 40-pulse averaged flow field. This script required over 24 hours to process 40 pulses for each of the eight phases.

Figures 4.19 and 4.20 compare phase-lock averaged and instantaneous iso-surfaces of constant vorticity magnitude for phases 2 and 4. Though some flow features are smoothed out by the phase locked averaging, it is clear that 40 pulses is insufficient to create a fully averaged flow field. This is particularly clear in Figure 4.19, taken in the middle of the pulse. It was learned, after pulsing simulations had

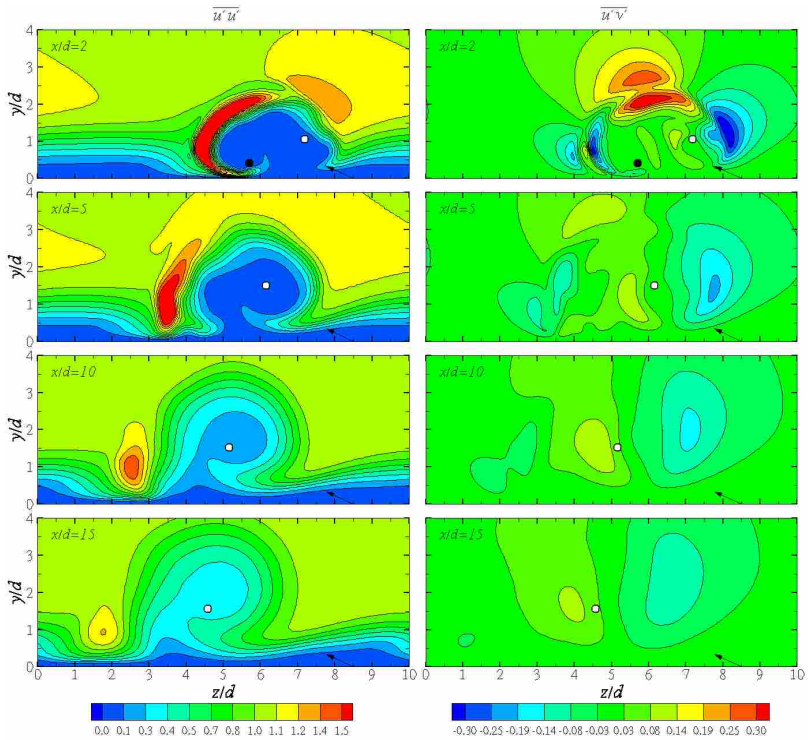

Figure 4.18: Contour plots of average numerical Reynolds stresses, $\overline{u'u'}/U_\infty^2$ (left column), and $\overline{u'v'}/U_\infty^2$ (right column), at various x/d planes.

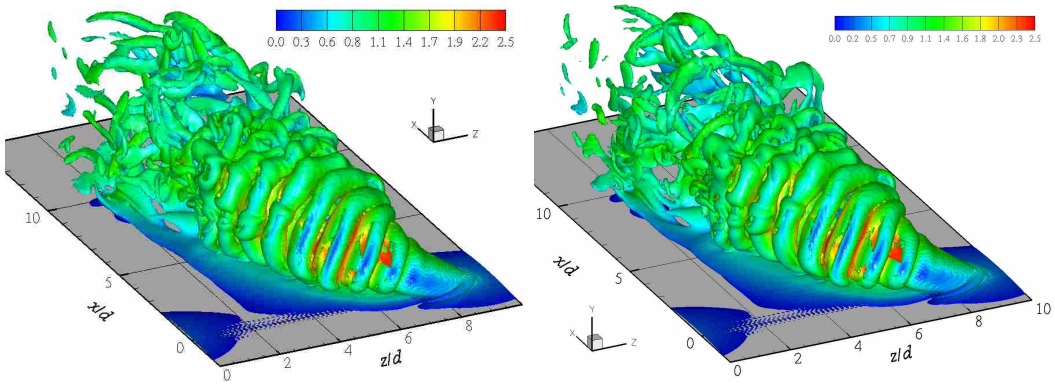

(a) (b)

Figure 4.19: Iso-surfaces of phase-lock averaged and instantaneous vorticity magnitude, $\overline{\omega}_{mag}d/U_\infty$=2, colored by velocity magnitude at phase 2. 40-pulse average (a), instantaneous (b)

almost concluded, that one of the primary reasons for utilizing phase locked averaging was to minimize experimental variation from pulse to pulse. These variations resulted from inconsistencies in the pulsing valve, variable particulate concentration

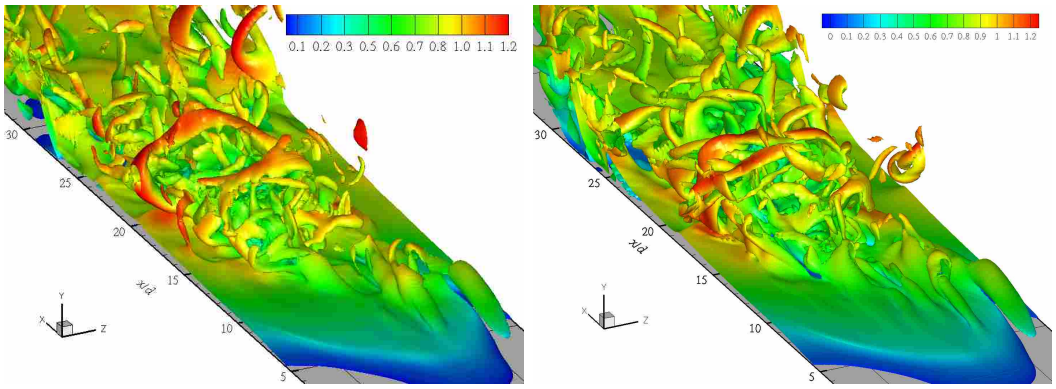

(a) (b)

Figure 4.20: Iso-surfaces of phase-lock averaged and instantaneous vorticity magnitude, $\overline{\omega}_{mag}d/U_\infty$=1, colored by velocity magnitude at phase 4. 40 pulse average (a), instantaneous (b)

passing through the laser sheet at a given instant, or general free stream fluctuations. Obtaining an averaged flow field at a given phase was a useful byproduct of the averaging process. The absence of such experimental variations in the numerics results in almost identical flow fields from pulse to pulse, particularly in phases 1-3. Though fluid structures for phases 4-8 are more randomly distributed traveling downstream, 40 pulses remains insufficient for analysis of fully averaged flow. Comparison with experimental data as done in Section 4.2, is therefore not feasible.

Instead, a brief qualitative comparison between the phase locked data and experiments will be performed. Figures 4.21 and 4.22 show contour plots of the streamwise velocity component at z/d=5 for phases 2 and 4. Though the differences between the averaged and instantaneous flow fields are obvious, the height of the jet-influenced zone subjected to an increased blowing ratio from the steady jet case, compares well with the experiments. The trough in the experimental velocity field at x/d=2 in Figure 4.21 corresponds to the acceleration region of the free stream fluid around the jet fluid, observed in Figure 4.6. Also of note are the x/d dimensions of the wake zones for each phase. At phase 2, the jet fluid still hasn't reached the $20d$ point but is slightly influencing the downstream boundary layer. By phase 4, a large portion of the jet fluid has convected out of the data window and the boundary layer

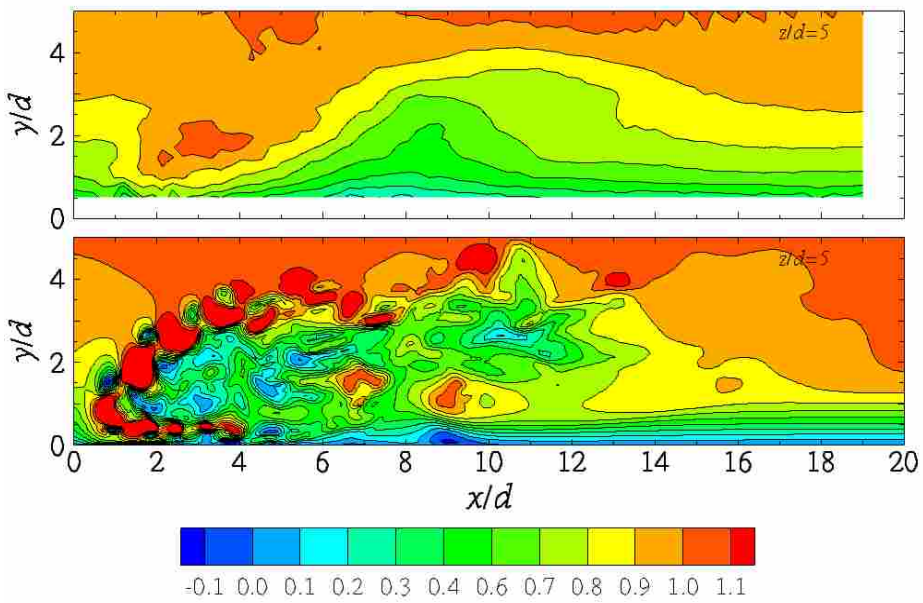

Figure 4.21: Comparison of average experimental and instantaneous numerical contour plots of streamwise velocity, u/U_∞, for phase 2 at z/d=5. Experiment in top plot.

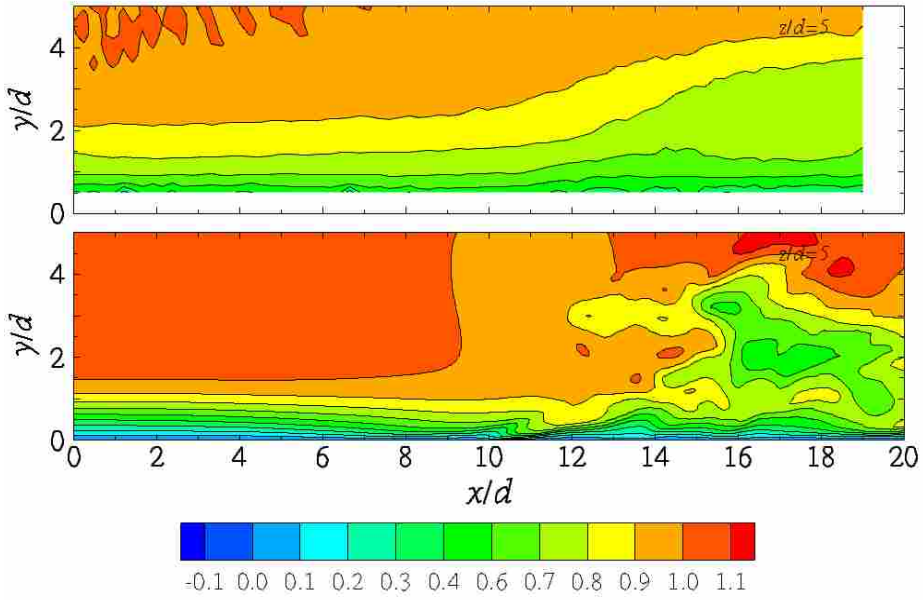

Figure 4.22: Comparison of average experimental and instantaneous numerical contour plots of streamwise velocity, u/U_∞, for phase 4 at z/d=5. Experiment in top plot.

is beginning to recover. In both figures, the velocity magnitudes in the wake region at each phase also agree well. The convection distances of the wake also demonstrate the temporal accuracy of the solver.

Because of the lack of time averaged data, and considering the transient nature of a pulsed jet, the opportunity to observe instantaneous flow features of the VGJ arises. Various flow visualization experiments have been performed on cross flow jets at these Reynolds numbers [8, 22, 23]. Figure 4.23 shows the instantaneous flow field around one such jet, obtained by New et al. [23]. Though all experiments focused on wall-normal jets, similarity between experiment and the numerics (Figure 4.19) can be seen in the formation of vortices wrapping around the jet fluid. These structures

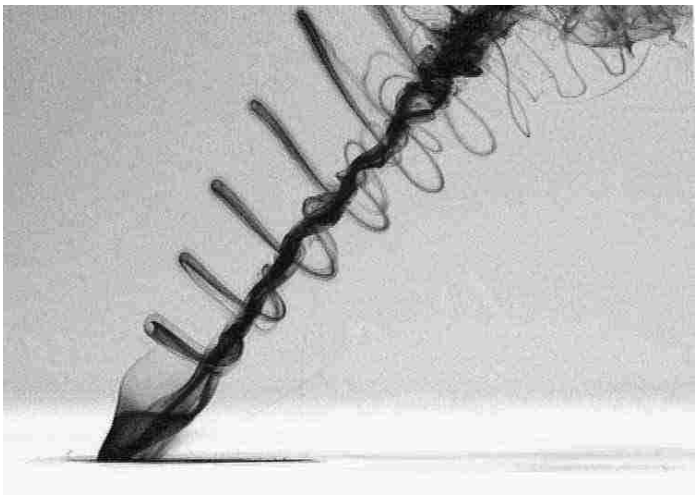

Figure 4.23: Flow visualization of wall-normal elliptical jet by New et al. [23].

form at the leading edge interface of the jet fluid and the free stream, and always merge with a primary counter-rotating vortex pair. This merging is indicated by the turbulent conditions seen at the uppermost region of Figure 4.23 and is also observed in Figure 4.19. The experiments describe these vortical rings as "kidney" and "anti-kidney" vortices and are observed at varying degrees of complexity depending on the flow conditions.

A key difference between the experiments and the simulations is the proximity of the jet fluid to the wall. This not only eliminates the symmetry present in a wall-normal jet but, combined with the pitch angle of the VGJ, restricts downstream vortical structure to a single primary vortex as opposed to a counter-rotating pair. These differences aside, kidney vortices are seen forming around the top edge of the jet fluid as it exits the hole, in Figure 4.24. This plot shows vorticity magnitude contours from an instantaneous flow field from the steady jet simulation at a vertical height of y/d=1.0. The vortices are characterized with strong cores and convect downstream in pairs. Each vortex in the pair forms independently of the other on the upstream and downstream sides of the jet fluid. No periodic oscillation occurs in this shedding process as it does in cross cylinder flows. The flow features in this domain slice agree particularly well with other flow visualization experiments performed by Haven and Kurosaka (not shown) [8].

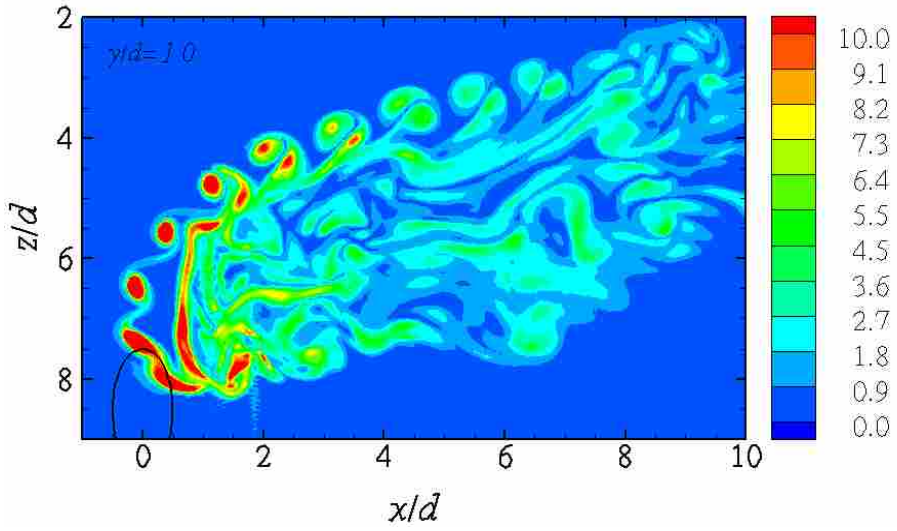

Figure 4.24: Contour plot of instantaneous numerical vorticity magnitude, $\overline{\omega}_{mag}d/U_{\infty}$ at y/d=1.0, showing vortical structures surrounding jet fluid.

The same study by Haven and Kurosaka [8] attributed the formation of these kidney vortex rings partially to vorticity generated by the hole wall, before exiting into the free stream. The use of a Dirichlet boundary condition for the VGJ hole

means that this source of vorticity is not present, thus most if not all of the vorticity seen at the jet fluid edge is due to the velocity gradient existing between the jet fluid and the free stream. Also of note is the fact that, when time averaged, these vortex rings construct the shell observed in Section 4.3 and account for the high turbulence levels inside the shell wall. The presence of kidney pairs accounts for the dual layer structure of the wall observed in Figure 4.15. The region of extremely low vorticity magnitude centered at x/d=0.5 and z/d=6.5 corresponds to the core jet fluid observed in Figure 4.16.

The vortex rings also possess a high streamwise rotational component, as indicated by the positive vorticity levels in the shell wall shown in Figures 4.8 and 4.14. This high level of vorticity is exceeded only by the primary vortex core and would indicate that though formed primarily by the velocity gradient at the jet fluid, large scale kidney vortex motion is dictated by streamwise vorticity induced by the jet fluid edge. This idea is supported when observing the shell wall wrapping around the top of the jet fluid and joining the primary vortex on the right side, before completely merging into one structure. Interestingly, New et al. [23] reported that variations on hole geometry and subsequent kidney vortex ring formation for wall-normal elliptical jets did little to change the primary vortex structure and wake for a steady jet.

Though unrelated, if a parameter such as hole shape does not significantly affect the downstream vorticity or wake production, how would these variables change with a pulsed jet? Furthermore, if the flows produce similar vorticity levels, how does a pulsed jet offer the same separation loss reductions accompanying a steady jet? Though not meant to be a definitive answer to this question, the idea was investigated by taking a time average of the flow field for only the on-time in the pulse period (6,250 time steps or 0.125 s of flow time). Streamwise vorticity at x/d=3 is plotted in Figure 4.25. This indicates that the primary vortex core almost reaches the vorticity levels obtained in the steady blowing case. Velocity vector plots (not shown) confirmed the presence of primary and secondary vortices. Without the constant momentum injection of the steady jet, vortex strengthening ceases though it remains a dominant flow feature downstream of the jet hole. Figure 4.22 shows that by phase 4 most of the

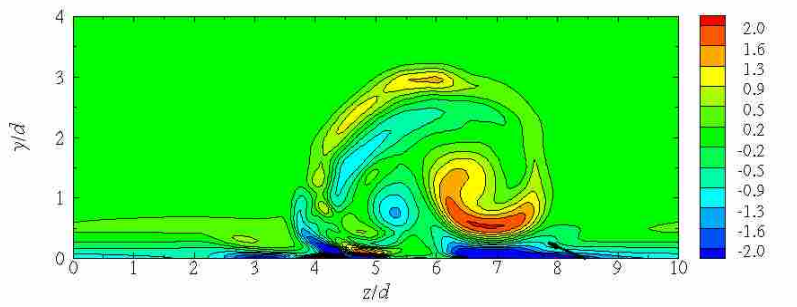

Figure 4.25: Contour plot of streamwise vorticity, $\overline{\omega}_x d/U_\infty$ at x/d =3, time-averaged for a single pulse.

jet fluid has convected out of the experimental data window and in order to further observe the primary vortex, later phases in the numerical results were analyzed.

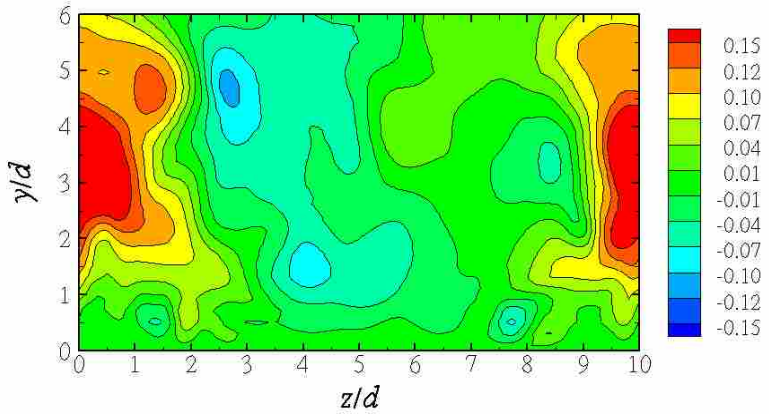

Figure 4.26: Phase-lock averaged contour plot of wall-normal velocity, $\overline{v}/U_\infty$, for phase 6 at x/d=45.

Phase locked averaging did not sufficiently change streamwise vorticity distributions, though the wall-normal velocity component was affected to a small degree and can be a strong indicator of vortex motion. Figure 4.26 was taken from phase 6 at x/d=45, which is just over twice the downstream length of the experimental data window. Accounting for the periodicity in the spanwise direction, there are well defined upwash and downwash regions in the flow field that would indicate the presence of a vortex. The magnitudes of these regions at this x/d location are greater

than those observed in the steady jet, which could be explained by the increased blowing ratio. The wide spread of the vortex indicates that its core is dissipating, as expected. Later phases (7 and 8) do not show any defined regions of wall-normal velocity, which could be due to the coarse mesh used in this region. A more likely scenario is that the vortex has mostly dissipated since the mesh resolution does not drastically change at these streamwise locations. The above analysis indicates that a significant primary vortex does develop with a pulsed jet but does not maintain structure as far downstream without a steady momentum injection.

Chapter 5

Adverse Pressure Gradient

5.1 No Control

As in the ZPG simulation (Section 4.1), a no-control case was evaluated to match the experimental conditions of the APG without jet actuation. The medium resolution mesh was again chosen because of the increased cell count incurred when including the wedge configuration. Confidence in this decision was based on the ability of this mesh to simulate the same flow features observed in the fine mesh, as discussed in Section 3.3.3. Because of free stream acceleration in the throat region, the inlet velocity and time step were reduced to ensure solver stability. This resulted in a CFL number of 0.3, not accounting for the VGJ. Detailed discussion of the mesh can be found in Section 3.2.2.

Though the wedge was the primary component for inducing laminar separation, the suction boundary discussed in Section 2.2 was a crucial element to separation zone behavior. Suction was applied to prevent flow separation just aft of the throat, which otherwise would interfere with the flow along the flat plate.

The suction boundary was simulated with a Dirichlet velocity boundary. Velocity components in the x and y directions were specified such that the velocity magnitude was normal to the suction boundary and directed away from the free stream. The level of suction required to create a separation zone similar to that measured in the experiments, was found iteratively. A similar process was used in the experiments and also consisted of shifting the wedge position in the x direction, relative to the leading edge of the flat plate. For the numerical simulations, the wedge was left at the position used in the experiments.

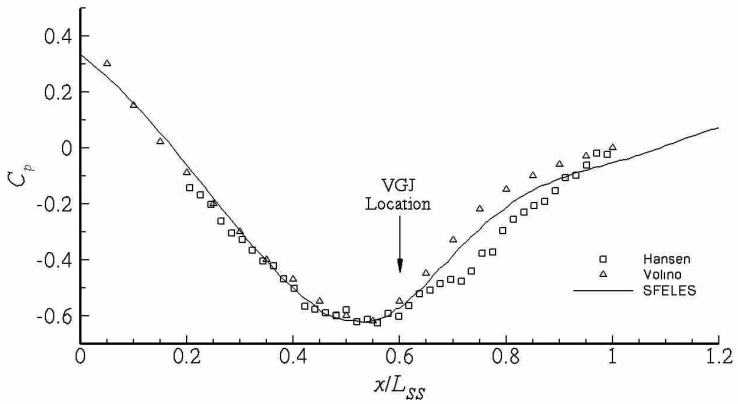

Figure 5.1: Pressure coefficient distribution for APG simulations [1, 16].

Table 5.1: Laminar separation zone dimensions.

	Separation (x/d)	$\overline{u}_{0.5}$ @ x/d =20 (y/d)	$\overline{u}_{0.9}$ @ x/d =20 (y/d)
Experiment	6.0	2.2	4.4
SFELES	5.7	2.6	3.4

The final pressure coefficient distribution plotted versus the x location, scaled by test section length L_{ss}, is shown in Figure 5.1. This was calculated from Eq. 2.1 and was based on a boundary layer edge velocity measured at $15d$ above the flat plate. The exit velocity was extracted from the time averaged mid-channel location at the outlet. This distribution yielded the separation zone dimensions in Table 5.1. Reasonably good agreement with the experiment is present in the numerical simulation.

It was found that increasing the suction force in the numerical simulations significantly moved the separation point upstream along the plate wall while, to a lesser degree, also increased the zone height downstream. Decreasing suction force had the opposite effect on separation zone dimensions. This relationship indicates that increasing suction serves to increase the adverse pressure gradient. Matching the experimental separation point in the x direction was the primary focus when iterating on the velocity components. This focus was based on two factors; the first being to match the x distance of boundary layer growth from the leading edge of the plate. Second, was to facilitate the simulation of momentum levels, mainly of the

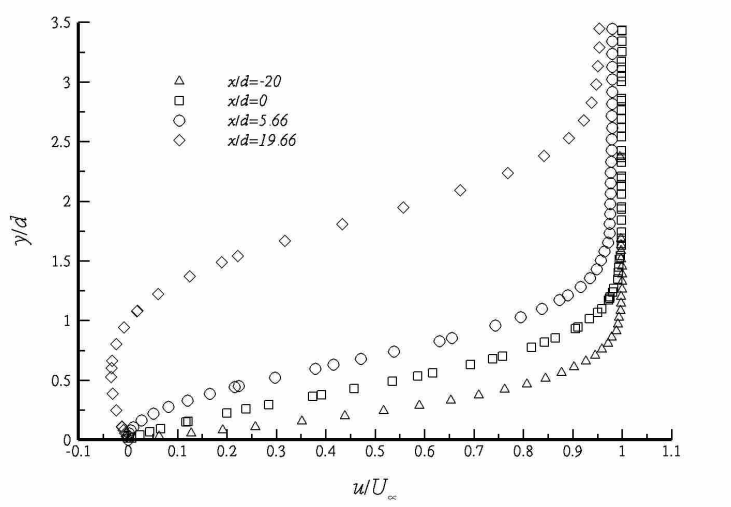

Figure 5.2: Time and spatial-averaged numerical boundary layer profiles at various x/d locations along flat plate, subjected to APG.

jet fluid incident on the separation zone, having been entrained by the free stream. Separation location in the numerics was measured by the first zero-crossing of the wall shear stress plot along the plate wall.

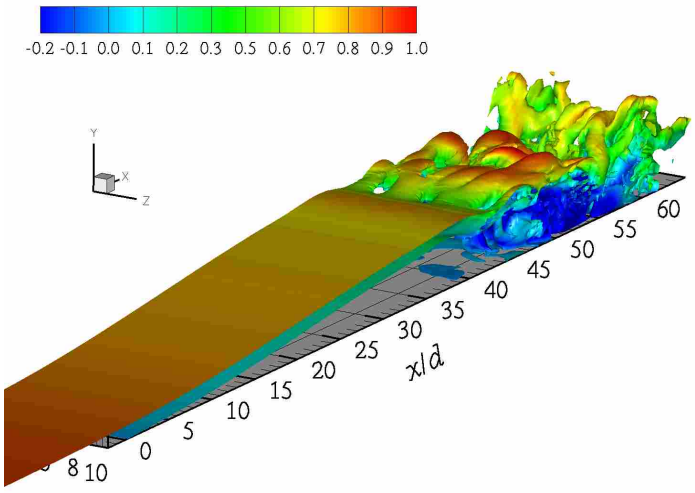

Figure 5.3: Instantaneous iso-surface of numerical vorticity magnitude, $\overline{\omega}_{mag}d/U_\infty$=0.6, colored with streamwise velocity for no-control APG case.

Time and spanwise averaged velocity profiles at various x/d locations are plotted in Figure 5.2. The laminar boundary layer at the jet is reduced in size by slightly over $0.5d$ compared to the ZPG case. The difference in boundary layer size is the result of the compression by the wedge on the free stream. The combination of a reduced boundary layer height and a reduction in inlet velocity resulted in a maximum y^+ of ~ 1, leading up to the VGJ boundary. An iso-surface of vorticity magnitude colored by free stream velocity is shown in Figure 5.3. The numerical separation zone is completely laminar up to x/d=40 where a transition to turbulence occurs. Similarly, turbulence was never observed in the experimental data window of $20d$ downstream of the jet. Also of note in the averaged numerical flow field was reattachment of the flow shortly after transition. This occurred at x/d=58, very near the beginning of the coarsely meshed vortex dissipation zone, at $60d$.

5.2 Pulsed Jet

Pulsing was initialized at a frequency of 1 Hz and a duty cycle of 25%, from the no-control case. The blowing ratio was increased to three, where the free stream velocity was extracted above the jet boundary from the no-control case. In addition to the eight phase locations analyzed in the experiments, instantaneous flow field snapshots at 37 additional points were recorded during 1.3 pulse periods.

Figure 5.4 shows iso-surfaces of vorticity magnitude colored with velocity magnitude at t/T=0.15. The jet pulse starts at t/T=0 and ends at 0.25. Differences in the flow field, when subjected to the APG, are readily visible in the kidney vortex rings looping around the jet fluid. They form closer to the jet hole and do not maintain the coherent structure present in the ZPG case. Proximity to the jet hole is likely due to the increase in blowing ratio, and thus velocity gradient at the jet fluid. Downstream, the rings dissipate sooner and the decay of coherent structures is more pronounced.

The APG also distorts the wake downstream of the jet. The jet fluid rises higher and covers a greater spanwise area than that observed in the ZPG case. The wake also maintains vorticity levels a greater distance downstream. This is expected, in light of the decreased stability of the laminar flow in the unfavorable pressure

gradient. Another subtle difference between the pressure gradient conditions is the increased size of the boundary layer roll-up vortex just upstream of the jet fluid. The spanwise extent of this vortex increases by approximately $2d$, from the ZPG case. Figure 5.5 shows iso-surfaces of normalized streamwise velocity colored with wall

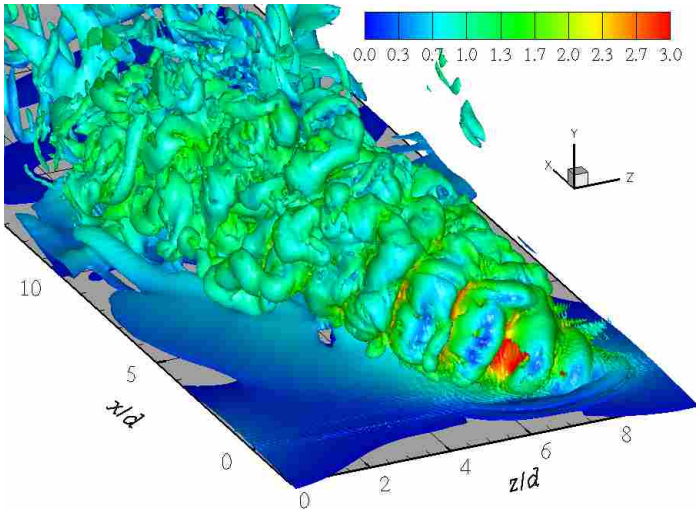

Figure 5.4: Instantaneous iso-surface of numerical vorticity magnitude, $\overline{\omega}_{mag}d/U_\infty$=2.0 at t/T=0.15, colored with velocity magnitude for APG case.

normal velocity at various locations in the pulse history, indicated in the upper left corner of each plot. The laminar separation zone before jet actuation is plotted in the upper left frame and the zone just before a subsequent pulse is in the bottom right frame. The leading packet of jet fluid to reach the separation zone resides primarily above the shear layer. This serves to weaken the separation zone and the remainder of the jet fluid is able to flush the low momentum separation fluid out of the domain.

Though primarily a 3-D structure, the jet also imposes 2-D influences on the flow field. The initial 2-D disturbance is visible in the separation zone at t/T=0.18. The separation zone has been flattened across the entire span of the domain. This size reduction occurs not only in the region directly affected by the jet fluid, but directly downstream of the jet hole where there is no jet fluid. The flattening extends downstream to approximately $15d$ though the jet influence on the separation zone is

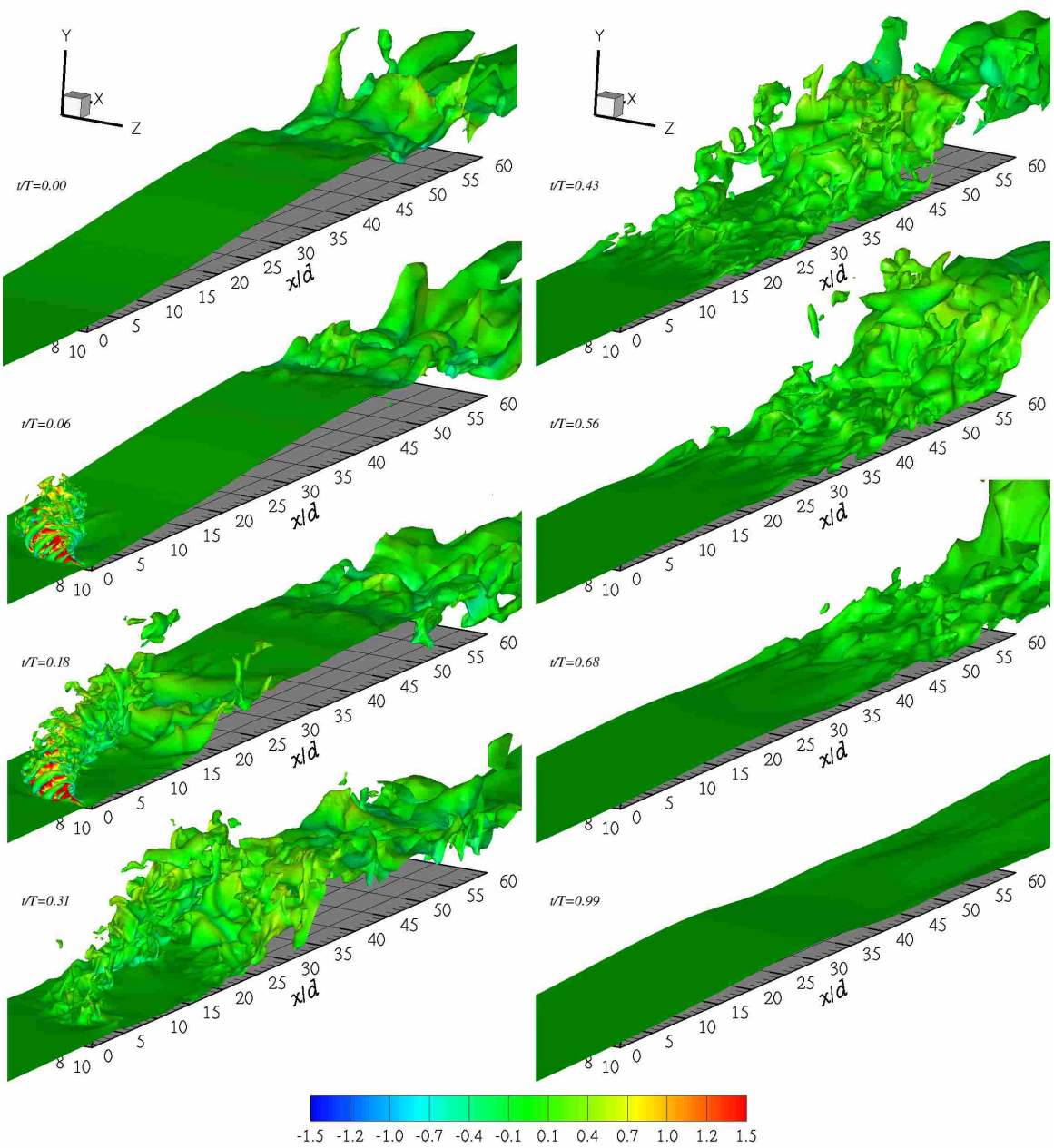

Figure 5.5: Instantaneous iso-surfaces of numerical streamwise velocity, $\overline{u}/U_\infty$ =0.5, colored with wall-normal velocity, showing various points in APG pulse period.

present to a lesser degree up to $25d$. It is clear that the jet dominates the upstream region of the separation zone and the flattening effect is likely due to the sudden mass flux of the jet pressing down on the shear layer, which responds in a spanwise uniform manner.

By t/T=0.31, the jet fluid has cleared away most of the separation zone up to $25d$. Though elements of the jet wake extend downstream to the turbulence transition point, the bulk of the separation bubble has remained intact. At t/T=0.68 the separation bubble has been eliminated and the remainder of the jet fluid is convecting out of the domain.

At t/T=0.99 there is an obvious lack of separation regrowth before the next pulse. This phenomenon was observed in the experiments and the level of regrowth at the $20d$ point is comparable, though slightly reduced, to that in the PIV data. This effectively results in two distinct separation reduction scenerios: first, are the effects of the initial pulse on an undisturbed laminar separation zone and second, are the effects of follow-up pulses on the significantly reduced separation zone. Each scenario will be discussed below.

5.3 Initial Pulse

Initial disturbance of the separation region by the leading packet of jet fluid is visible in contour plots on the z/d=4 plane, of normalized spanwise vorticity shown in Figure 5.6. The mass being squeezed out of the flattened upstream separation zone, combined with the mass flux imparted by the jet on top of the separation zone, generate a strong negative-sign vortex ($x/d \approx 17$ at t/T=0.15) which remains primarily in the shear layer and never reaches the wall. This vortex is the first notable disturbance directly in the shear layer but does not convect the entire distance downstream. Instead, various smaller shear layer vortices form as the first dissipates. The passage of these vortices coincides with the complete dissolution of the shear layer which is followed by the jet fluid flushing the remainder of the separation zone.

It appears that a large portion of the pulsed VGJ efficacy on the undisturbed separation zone is due to the formation and propagation of these shear layer vortices. The first vortex is initially a 2-D disturbance and covers most of the spanwise extent of the domain, as shown in the iso-surface plot in Figure 5.7. The vortex is represented by the thick tube extending slightly diagonally between x/d=20 on the right side of the plot to x/d=18 on the left. Vortex roll up is visible in the "V" shape appearing in

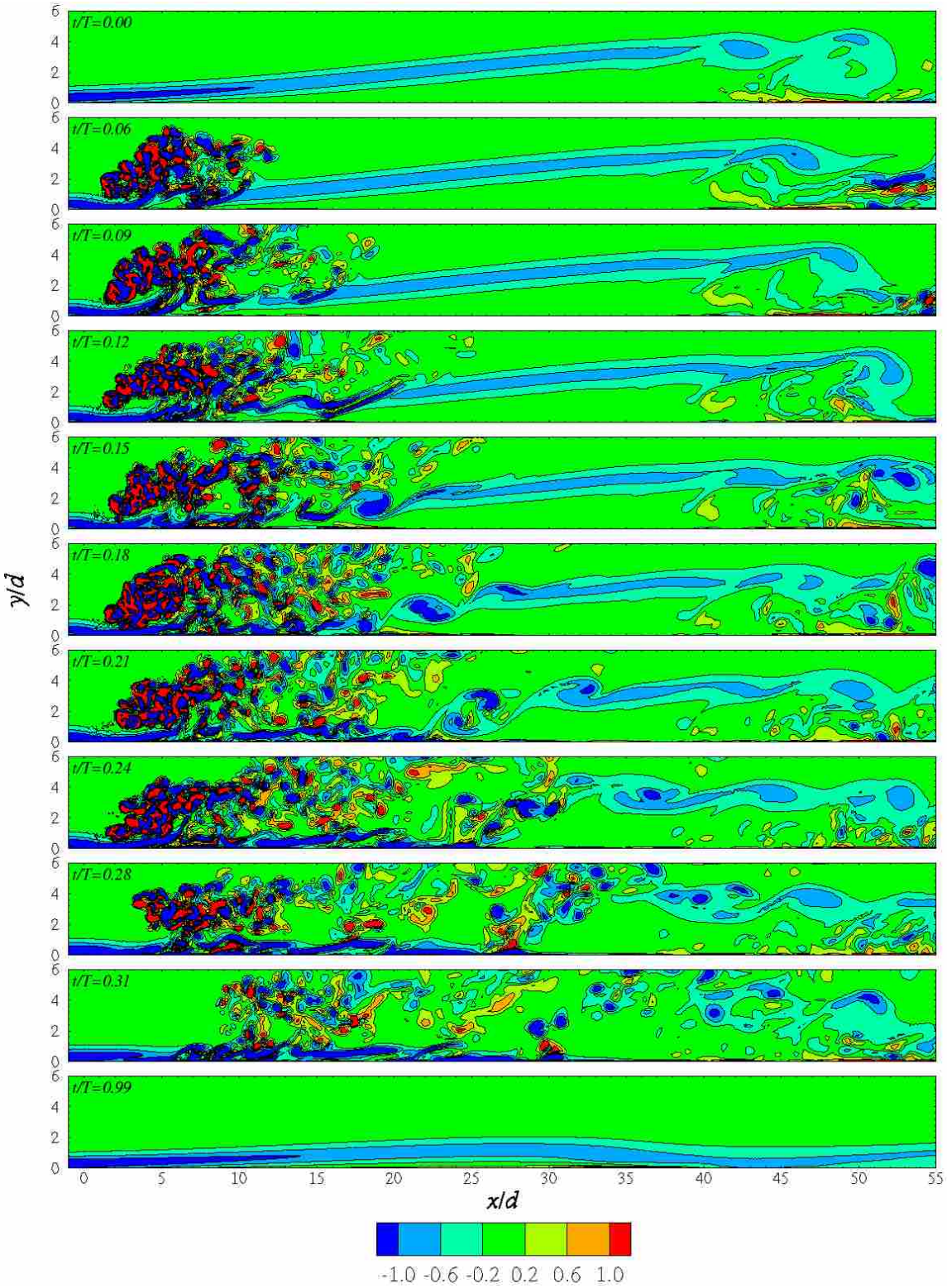

Figure 5.6: Instantaneous contour plots of numerical spanwise vorticity, $\overline{\omega}_z d/U_\infty$ at z/d=4, showing various points in APG pulse period.

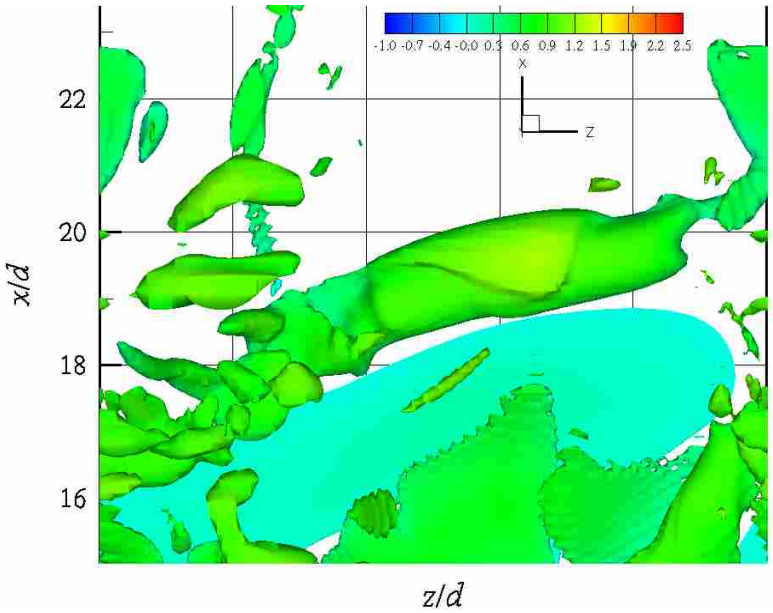

Figure 5.7: Instantaneous iso-surface of numerical spanwise vorticity, $\overline{\omega}_z d/U_\infty$=1.3, colored with streamwise velocity, at t/T=0.15. Perspective is looking down on jet (not in plot range).

the middle of the tube. The diagonal orientation of the tube is due to the presence of the jet wake passing above and on the left of the core. Though the jet fluid distorts the vortex structure directly beneath it, the core remains intact. A side view of the undisturbed vortex can be seen in Figure 5.8 showing planes shifted to z/d=7. The sporadic vortical structures appearing in the flow field at t/T=0.21, just above the vortices is fluid from the neighboring jet. Two dimensional disturbances in the separation zone, likely related to these vortices, were observed numerically by Postl et al. [12] and were one of the key indicators for their investigation into the use of natural shear layer frequencies to induce instability in the laminar separation zone.

The influence of this vortex on the flow field is consistent with the findings of Bons et al. [2] who theorized that the key to pulsed jet efficacy appeared to result from events linked to the beginning and end of the jet pulse, as opposed to the bulk massflow of the jet fluid. This was observed based on measuring similar integrated wake loss coefficients in an LPT cascade for a variety of frequencies and duty cycles. It is feasible that shorter bursts (lower duty cycle) of fluid at sufficient blowing ratios would create a similar shear layer vortex and obtain the same weakening effect. This

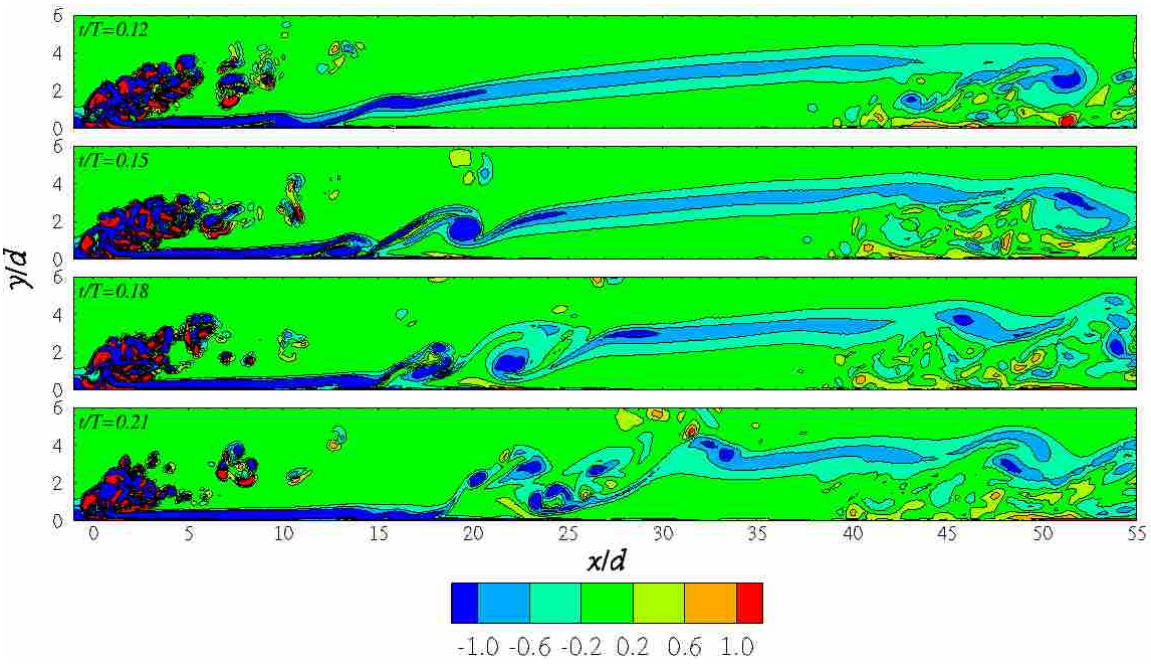

Figure 5.8: Instantaneous contour plots of numerical spanwise vorticity, $\overline{\omega}_z d/U_\infty$ at z/d=7, showing various points in APG pulse period.

is further supported when considering where the first vortex lies in relation to the jet fluid. In Figure 5.6 at t/T=0.15, jet fluid can be seen above and ahead of the shear layer vortex. This packet of fluid leads the vortex because by this point in time, it has been pulled up by the APG and entrained with the accelerated free stream flow in the throat; its effect on the separation zone appears largely negligible.

There is little evidence that a primary vortex structure, formed as a direct consequence of the jet fluid, is the mechanism which mitigates separation in these flow conditions. It has been shown in the ZPG case that a pulsed jet at this duty cycle does indeed produce a primary vortex. In fact, in the following section, an attempt will be made at confirming this for the APG flow field with the instantaneous results in the presence of a weaker separation zone. However, the 2-D nature of both the upstream flattening of the separation zone and the initial shear layer vortex do not support the idea that the primary vortex is the dominant mechanism in this case. This is further supported by the apparent inability of the jet fluid to penetrate the separation zone until after the latter has been weakened, which indicates that the

vortex is not initially in a position (because of the upward pull of the APG) to affect the undisturbed separated flow.

Furthermore, as noted in Figure 5.4, the vortical structures formed by the pulsed jet in the APG appear to transition quickly to turbulence. The passing of the bulk of this apparently turbulent flow, in the absence of a structured separation zone, coincides with flow reattachment to the wall. Though not confirmed numerically with turbulent statistics, this analysis of the instantaneous flow features seems to agree with recent studies indicating that transition is the primary reattachment mechanism for pulsed VGJs at these blowing ratios [24].

5.4 Follow-Up Pulse

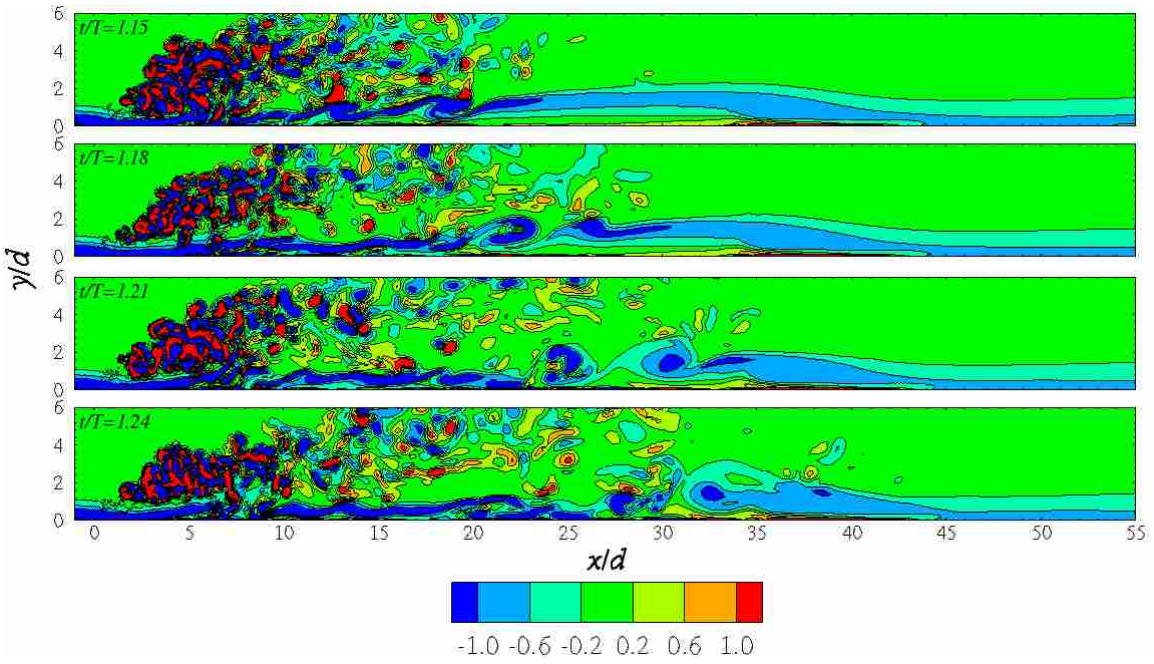

Figure 5.9: Instantaneous contour plots of numerical spanwise vorticity, $\overline{\omega}_z d/U_\infty$ at z/d=4, showing various points in APG follow-up pulse period.

Figure 5.9 shows a sequence of spanwise vorticity plots at z/d=4. The significantly reduced separation zone is visible downstream of x/d=20 at t/T=1.15. Formation of a shear layer vortex is again visible (x/d ≈17 at t/T=1.15) but this

time it is smaller and weaker. By virtue of the reduced height of the shear layer, it forms virtually at the wall surface. The vortex does not propagate as far downstream as in the full separation conditions because of the reduced mass flow being pushed out of the upstream separation zone as well as viscous interaction with the wall. The bulk jet fluid extends vertically the same distance as in the initial pulse at this point in time, but in the absence of the full separation zone, also extends closer to the wall.

A pulse-on disturbance of the flow field is still present, but the vortices are mostly three-dimensional and do not extend the full span of the domain. When considering the size dominance of the jet fluid over the reduced separation zone, the importance of these vortices and their effect on the shear layer decreases. Again however, this readily suggests that shorter jet bursts and reduced blowing ratios would be just as effective for follow up pulses at these flow conditions.

Though there is a lack of time averaged data for this flow field to fully evaluate primary vortex formation and impact, Figure 5.10 shows an instantaneous contour plot of streamwise velocity at t/T=1.18 and x/d=15. The lobe shape of the velocity field is very similar to those observed in Chapter 4. In the center of the lobe there is a streamwise momentum deficit and the flow near the wall on the right and left sides show boundary layer fluid mixing with the free stream. An increase in vertical height is apparent, primarily due to the APG influence. There is also increased spanwise drift as compared to the ZPG cases, likely due to the increased blowing ratio. This plot strongly suggests that a large vortex does form downstream of the jet hole.

Figure 5.11 shows contour plots of positive (white) and negative (black) wall shear stress along the flat plate at various times during the follow up pulse. Instantaneous turbulent flows (jet wake) may not accurately indicate all attached regions, but general trends are still visible. At t/T=1.03 the jet has just initiated and the reduced separation zone is visible between x/d=12 and 40. By t/T=1.28 the jet has turned off and much of the separation zone has been eliminated. Of note is the separation bubble directly downstream of the jet hole, visible in the first two plots, resulting from the core jet fluid blocking the free stream. Small pockets of separated flow existing inside predominantly attached flow regions are attributed to vortical structures in the

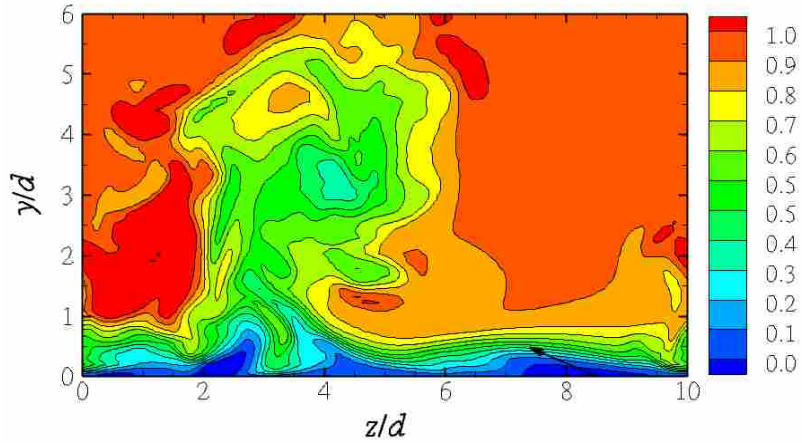

Figure 5.10: Instantaneous contour plot of numerical streamwise velocity, u/U_∞, at x/d=15 and t/T=1.18.

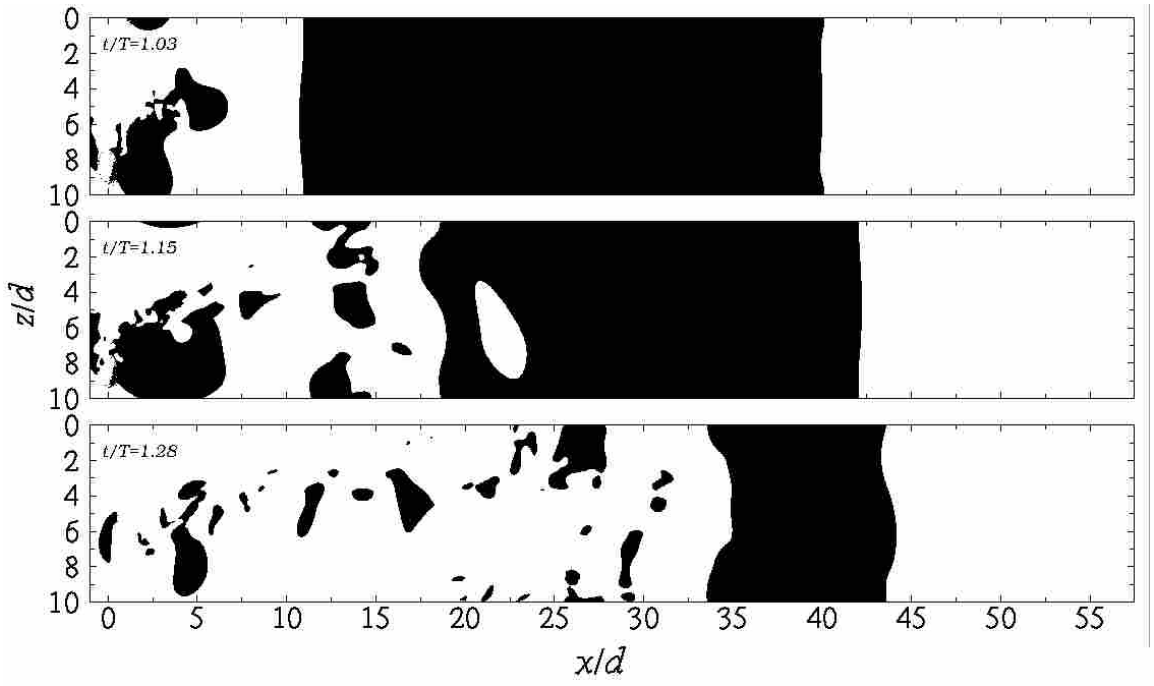

Figure 5.11: Instantaneous contour plots of numerical wall shear stress with contour levels indicating positive (white) or negative (black) shear stress.

jet wakes (including the neighboring jet) convecting downstream. The attached flow regions induced by the jet seem to be mostly two-dimensional. Similar trends were observed for the initial pulse plots of the same variable.

Further analysis is certainly necessary to ascertain which flow disturbance might be more critical to separation reduction: vortical motion or turbulent transition. Various factors seem to point to both scenerios. Even in the presence of a large 3-D disturbance (the primary vortex), the flow field attaches to the wall in a 2-D manner. As mentioned previously, the spanwise spread of the jet wake is increased due to the APG and iso-surface vorticity plots point to a rapid breakdown of any structures in the jet wake which would indicate a wide spread turbulent transition. Conversely, a large vortical structure is almost certainly present which dominates both the upstream portion of an undisturbed separation layer and the entire reduced separation layer.

For either mechanism, the importance of the pulse-on shear layer disturbance appears critical to eliminating the laminar separation, particularly with an undisturbed separation layer. If the shear layer weakening process is the most crucial component, duty cycle could potentially be reduced to a point where vortex formation is insignificant and transition is the primary mechanism. In such a scenerio, blowing ratio would remain an important factor because of the physical position of the jet mass flux in relation to the separation zone, which helps create the pulse-on disturbance.

Chapter 6

Conclusions

Numerical simulations of PIV experiments conducted with VGJs on a flat plate at a Reynolds number based on plate length of 50,000, were performed for three flow conditions using a time-accurate hybrid Navier-Stokes solver. The solver utilizes a second order finite element method in the xy plane and a Fourier method in the z direction, with second order temporal accuracy. A boundary condition was developed to simulate a spanwise periodic row of VGJ holes.

Steady blowing subjected to a zero pressure gradient at B=2 yielded excellent agreement with experimental PIV data, as shown in time averaged contour and iso-surface plots. A large vortex, observed with various flow variables, dominates the flow field downstream of x/d=5. Detailed analysis of the numerical results was conducted showing a shell region surrounding the primary and secondary vortex cores, before merging with the primary vortex. Vortical mixing of boundary layer fluid with free stream fluid was also observed.

Pulsing in the zero pressure gradient was initialized from a no-control case. A non-dimensional pulsing frequency of 0.34 and duty cycle of 25% was matched from the experiments. Phase locked averaging was performed over 40 pulses but did not yield sufficiently averaged data for a direct comparison with experimental results. A qualitative comparison between averaged experimental and instantaneous numerical results was performed with good agreement. The phase locked flow fields did however, confirm the production of a primary vortex by the reduced mass flow of the pulsed jet. Analysis of the instantaneous numerical flow field agreed well with various flow visualization experiments which described the formation of "kidney" vortices forming around cross-flow jets. These vortices result mostly from the velocity gradient between

the core jet fluid and the free stream and form rings around the jet before merging with the primary vortex.

An adverse pressure gradient was applied to the flat plate by simulating the experimental wedge configuration. After demonstrating good agreement between experiments and numerical simulations of the no-control laminar separation zone, the jet was pulsed at the same experimental settings for the zero pressure gradient for 1.3 pulses. Instantaneous flow fields were recorded at various locations in the pulse history. After the initial pulse, the separation zone never recovered to its original size.

For the initial pulse, spanwise vorticity plots show a series of strong negative vortices in the shear layer of the separation zone. This pulse-on sequence convects with the leading packet of jet fluid and significantly weakens the shear layer, allowing the bulk jet fluid to flush the separated zone out of the domain. Follow up pulses generate smaller and weaker vortices that also propagate in the shear layer. However, the follow-up pulse dominates the reduced separation layer and the importance of these vortices lessens. It is reasonable to assume that reduced blowing ratios and duty cycles would produce similar shear layer vortices and similar loss reduction scenerios for either separation zone.

Instantaneous flow field plots point to both the existence of a large primary vortex, as well as rapid transition to turbulence, when subjected to the adverse pressure gradient. Various 2-D flow disturbances were noted in during the pulse and wall shear stress plots indicate that separation reduction occurs two dimensionally. These observations seem to point to both mechanisms playing a role in separation loss reduction though the presence of shear layer vortices seems to be a crucial component in both cases.

Further analysis of these flow fields would be necessary to discern the primary mechanisms behind separation reduction using a pulsed jet. Preliminary work might include analyzing the influence of increased spanwise resolution and further refinement of the wake region downstream of the jet. The mass flux requirements for generating the shear layer vortices could be analyzed by reducing the blowing ratio and duty cycle

and varying the pulse frequency. Turbulence levels could be analyzed by including other statistics such as intermittency. Also, further analysis of the numerical wedge configuration is needed. This includes mesh resolution analysis and more detailed observations of the effects of the suction boundary on the flow field.

Bibliography

[1] R. J. Volino and L. S. Hultgren, "Measurements in separated and transitional boundary layers under low-pressure turbine airfoil conditions," *ASME Journal of Turbomachinery*, vol. 123, no. 2, pp. 189–197, 2001. 1, 6, 7, 52

[2] J. Bons, R. Sondergaard, and R. B. Rivir, "Turbine separation control using pulsed vortex generator jets," *Transactions of the ASME*, vol. 123, pp. 198–206, April 2001. 1, 2, 9, 59

[3] J. Bons, R. Sondergaard, and R. Rivir, "The fluid dynamics of LPT blade separation control using pulsed jets," *Journal of Turbomachinery*, vol. 124, pp. 77–85, January 2002. 1, 2, 9

[4] M. Bloxham, D. Reimann, and J. P. Bons, "The effect of vgj pulse characteristics on separation bubble dynamics," *44th AIAA Aerospace Sciences Meeting and Exhibit*, pp. 1–14, January, 2006, Reno, NV AIAA 2006. 1

[5] Z. U. Khan and J. P. Johnston, "On vortex generating jets," *International Journal of Head and Fluid Flow*, vol. 21, pp. 506–511, 2000. 2, 37

[6] R. Sondergaard, M. Sucher, J. P. Bons, and R. B. Rivir, "Reducing low-pressure turbine stage blade count using vortex generator jet separation control," *Proceedings of ASME Turbo Expo*, pp. 1–7, June, 2002, Amsterdam, The Netherlands ASME 2002. 2

[7] G. S. Rixon, "Development of a steady vortex generator jet in a turbulent boundary layer," *Journal of Fluids Engineering*, vol. 125, pp. 1006–1015, November 2003. 2

[8] B. Haven and M. Kurosaka, "Kidney and anti-kidney vorticies in crossflow jets," *Journal of Fluid Mechanics*, vol. 352, pp. 27–64, 1997. 2, 45, 46

[9] L. L. Yuan, R. L. Street, and J. H. Ferziger, "Large eddy simulations of a round jet in crossflow," *Journal of Fluid Mechanics*, vol. 379, pp. 71–104, 1999. 2

[10] L. Jiang and C. Liu, "Direct numerical simulation for flow separation control with pulsed jets," *41st AIAA Aerospace Sciences Meeting and Exhibit*, pp. 1–33, January, 2003, Reno, NV AIAA 2003-0611. 2

[11] D. P. Rizzetta and M. R. Visbal, "Numerical simulation of separation control for a transitional highly-loaded low-pressure turbine," *2nd AIAA Flow Control Conference*, pp. 1–24, June 2004, Portland, Oregon 2004-2204. 2

[12] D. Postl, A. Gross, and H. F. Fasel, "Numerical investigation of low-pressure turbine blade separation control," *41st AIAA Aerospace Sciences Meeting and Exhibit*, pp. 1–12, January, 2003, Reno, NV AIAA 2003-0614. 2, 59

[13] D. Postl, A. Gross, and H. Fasel, "Numerical investigation of active flow control for low-pressure turbine blade separation," *42nd AIAA Aerospace Sciences Meeting and Exhibit*, pp. 1–13, January, 2004, Reno, NV AIAA 2004-0750. 2

[14] A. Gross and H. F. Fasel, "Simulation of active flow control for a low pressure turbine blade cascade," *43rd AIAA Aerospace Sciences Meeting and Exhibit*, pp. 1–18, January, 2003, Reno, NV AIAA 2005-0869. 2

[15] A. Gross and H. Fasel, "Investigation of low-pressure turbine separation control," *45th AIAA Aerospace Sciences Meeting and Exhibit*, pp. 1–15, January, 2007, Reno, NV AIAA 2007-0520. 2

[16] L. Hansen and J. Bons, "Phase-locked flow measurements of unsteady vortex generator jets in separating boundary layer," *Journal of Proplusion and Power*, vol. 22, no. 3, pp. 558–566, May 2006. 3, 5, 52

[17] L. Hansen, "Phase locked flow measurements of steady and unsteady vortex generator jets in a separating boundary layer," Masters Thesis, Brigham Young University, April 2005. 3, 5

[18] R. Eldredge, "Active control of a separating boundary layer with steady vortex generating jets : detailed flow measurements," Masters Thesis, Brigham Young University, April 2004. 5, 36

[19] D. O. Snyder and G. Degrez, "Large eddy simulation with complex 2-D geometries using a parallel finite-element/spectral algorithm," *International Journal for Numerical Methods in Fluids*, vol. 41, no. 10, pp. 1119–1135, 2003. 11, 12, 13

[20] D. O. Snyder, "A parallel finite-element/spectral LES algorithm for complex two-dimensional geometries," Ph.D. dissertation, Utah State University and Von Karman Institute For Fluid Dynamics, January 2002. 11, 13

[21] T. Nierhaus, J. Thomas, Y. Detandt, and D. Abeele, "Direct numerical simulation of bubbly taylor-couette flow," *Proceedings of the 4th International Conference on Computational Fluid Dynamics*, July 2006, Gent, Belgium. 13

[22] A. Perry and T. Lim, "Coherent structures in coflowing jets and wakes," *Journal of Fluid Mechanics*, vol. 88, no. 3, pp. 451–463, 1978. 45

[23] T. New, T. Lim, and S. Luo, "Elliptic jets in crossflow," *Journal of Fluid Mechanics*, vol. 494, pp. 119–140, 2003. 45, 47

[24] D. Reimann, M. Bloxham, J. Pluim, and J. Bons, "Comparison of spanwise wake and discrete jet disturbances on a separating low-pressure turbine blade," *45th AIAA Aerospace Sciences Meeting and Exhibit*, pp. 1–22, January, 2007, Reno, NV AIAA 2007. 61